Niobium aggregation and vacancylike defect evolution in nanostructured Nb-doped Mg: Their role in the kinetics of the hydride-to-metal phase transformation

C. Macchi,[1] C. Maurizio,[2] R. Checchetto,[3] S. Mariazzi,[3] L. Ravelli,[4] W. Egger,[4] P. Mengucci,[5] N. Bazzanella,[3] A. Miotello,[3] A. Somoza,[6] and R. S. Brusa[3]

[1]*IFIMAT, UNCentro and CONICET, Pinto 399, B7000GHG Tandil, Argentina*
[2]*Dipartimento di Fisica e Astronomia and CNISM, Università di Padova, Via Marzolo 8, I-35131 Padova, Italy*
[3]*Dipartimento di Fisica and CNISM, Università di Trento, Via Sommarive 14, I-38123 Trento, Italy*
[4]*Institut für Angewandte Physik und Messtechnik, Universität der Bunderswehr München, 85577 Neubiberg, Germany*
[5]*Dipartimento di Fisica e di Ingegneria dei Materiali, Università delle Marche, I-60131 Ancona, Italy*
[6]*IFIMAT, UNCentro and CICPBA, Pinto 399, B7000GHG Tandil, Argentina*

(Received 22 September 2011; revised manuscript received 15 March 2012; published 18 June 2012)

The structural evolution of nanostructured Nb-doped magnesium film samples and its correlation with the change of the H_2 desorption kinetics after successive H_2 sorption cycles at 623 K was investigated by different techniques. The variation of the dispersed Nb fraction and the Nb clusterization was followed by extended x-ray absorption fine structure (EXAFS), while the progressive Mg nanostructuring was monitored by x-ray diffraction. The presence of vacancylike defects and their evolution was studied using positron annihilation lifetime spectroscopy and Doppler broadening spectroscopies. It was found that, with successive H_2 sorption cycles: (i) the H_2 desorption kinetics progressively becomes slower until stationary conditions are reached and (ii) the Nb dopant atoms, dispersed in the nanocrystalline Mg layers, aggregate, forming nanoclusters. Our results show that the progressive Nb aggregation drives the H_2 desorption kinetics. EXAFS analysis show that fast desorption kinetics is due to the presence of small (∼1 nm) Nb aggregates rather than Nb atoms dispersed into the Mg matrix. With cycling, the Nb aggregates progressively grow, forming larger bcc Nb nanoclusters and the H_2 desorption kinetics becomes slower. In the as-deposited Nb-doped Mg samples, analysis of the positron data reveals the presence of intragranular vacancylike defects and of vacancy clusters which are inferred to be mainly located at the grain boundaries of the nanocrystalline Mg layers. With H_2 cycling: (i) a decrease of the atomic fraction of the intragranular vacancylike defects after the first two sorption cycles was observed, and (ii) an increase of the atomic fraction of vacancy clusters at grain boundaries and the appearance of vacancylike defects located at the interface between the Nb aggregates and the Mg matrix was probed. It was also found that the kinetics follows a nucleation and growth mechanism and, under stationary conditions, the Mg nucleation is controlled by vacancy-decorated bcc Nb nanoclusters rather than by vacancy clusters, as in undoped Mg samples.

DOI: 10.1103/PhysRevB.85.214117 PACS number(s): 78.70.Bj, 61.72.J−, 64.70.K−, 88.30.rd

I. INTRODUCTION

Among the first-order solid-solid phase transformations, the hydride-to-metal transformation in magnesium-based systems is of particular interest, magnesium hydride (MgH_2) being a promising material for hydrogen storage applications.[1] The release of hydrogen requires the transformation of the ionic MgH_2 compound (β phase) to the hcp Mg metal (α phase). Experiments indicate that the kinetics of MgH_2-to-Mg transformation is controlled by a nucleation and growth mechanism (NG): Mg nuclei form at extended defects of the matrix, such as grain boundaries, and their thermally activated growth is the rate-limiting step in the transformation kinetics.[2,3]

Research on Mg is aiming to reduce the high temperature required for the dissociation of its hydride phase and to accelerate the H_2 sorption kinetics, which is slow in MgH_2 even at temperatures as high as 600 K.[1–3] The use of nanocrystalline MgH_2 obtained by high-energy mechanical milling is a promising route.[2,3] The analysis of the x-ray diffraction (XRD) spectra of MgH_2 indicates that the milling process introduces extended defects and produces MgH_2 grain refinement, giving rise, after long milling times, to nanostructured powders: The improved H_2 desorption kinetics was thus attributed to the presence of extended defects which favor the Mg nucleation process and to the high density of grain boundaries acting as fast diffusion path for hydrogen atoms.[2,3]

The H_2 sorption kinetics can be accelerated also by using transition metals (TMs)[4] or transition metal oxides (TMOs)[5] as a milling additive. In spite of a large amount of experimental work on the role of the TM or TMO additives, a conclusive picture has not emerged regarding their catalytic action. In the form of nanoclusters TM and TMO additives can accelerate the H_2 sorption kinetics through different mechanisms: (i) when present at the Mg sample surface the nanoclusters catalyze surface processes involving hydrogen molecules;[6] (ii) when dispersed into the matrix they accelerate the kinetics acting as heterogeneous nucleation sites in the phase transformation[7] and facilitate the migration of H atoms dissociated from the hydride phase to the sample surface.[7–10]

In previous studies on samples where stationary desorption kinetics was reached, we observed that different additives reduce the characteristic desorption times by more than a factor of ten compared to that see with undoped Mg films and that the additive content controls the mechanism of the desorption kinetics.[11,12] In particular, detailed studies on the Nb catalytic capacity at dopant contents between 0.1 and 5 at. % were carried out. With dopant contents lower than 2 at. %, it was observed that the Nb atoms partially aggregate in

clusters with typical sizes around 10 nm and accelerate the sorption process acting as heterogeneous nucleation sites for Mg in the hydride-to-metal phase transformation.[7,12,13] When the Nb content is larger than 2 at. % a further mechanism operates: At this concentration, the average distance among the Nb aggregates is very short and drives the formation of a percolative network constituted by transformed Mg domains. In this percolative network, the H diffusion process is faster than that in the hydride matrix and the desorption process is thus accelerated.[13]

We also observed a remarkable difference between undoped Mg and Nb-doped Mg samples submitted to H_2 sorption cycles at 623 K. Starting with the as-deposited sample, undoped Mg samples exhibit a progressive acceleration of the H_2 desorption process after successive H_2 sorption cycles: Stationary kinetics is reached after about 9 cycles due to the progressive increase of the atomic concentration of vacancy clusters at the grain boundaries.[14] Conversely, in Nb-doped Mg samples the H_2 desorption process became progressively slower and stationary kinetics is attained after a number of cycles that depend on the Nb content.[12]

In this work, we present a study on the evolution, after successive hydride-to-metal phase transformations of the Mg matrix, of the chemical-physical state of the Nb additive and of vacancylike defects in nanostructured Nb-doped Mg films. The aim of the study is to understand the correlation between the structure of the hydride forming material at nanoscale level and the H_2 desorption kinetics and storage capacity as monitored by Sievert-type technique.[15,16] Toward this aim we have prepared self-supporting Nb-doped Mg films which are suitable because (i) the Nb concentration in the film samples can be properly tuned during the deposition stage and evaluated after deposition and (ii) the Nb aggregation process can be controlled by changing the additive concentration.

The evolution of Nb additive was studied by extended x-ray absorption fine structure (EXAFS), while the evolution of vacancylike defects was studied by positron annihilation spectroscopy (PAS).

Experiments on very small clusters embedded in the matrix are challenging, since few-atom aggregates are poorly detected by XRD or by electron microscopy. EXAFS spectroscopy is an ideal tool to investigate the aggregation steps of atomic additives in a matrix such as Mg since it makes it possible to detect both the fraction of the dispersed dopant and the presence of aggregates, even if they are small sized.[7,17] Up to now, the effectiveness of small dopant clusters (size in the one- to few-nanometer range) and/or dispersed dopant atoms in controlling the H_2 kinetics has not been experimentally studied. This issue is of utmost interest because theoretical calculations suggest that the presence of TM atoms into the MgH_2 matrix reduce the activation energy for hydrogen desorption[18,19] and decrease the heat of MgH_2 formation.[20,21]

The information on the vacancylike defect evolution was obtained by using two variants of PAS, namely positron annihilation lifetime spectroscopy (PALS) and coincidence Doppler broadening (CDB) spectroscopy. The type of vacancylike defects, from monovacancies to vacancy clusters, was revealed by PALS. The chemical identity of the atoms surrounding such defects was extracted from the CDB data. To discuss PAS data, PALS and CDB results on undoped Mg samples are also reported. Furthermore, *ab initio* calculations were carried out to obtain the lifetime values of trapped positrons in monovacancies of Mg and in monovacancies of Mg decorated by oxygen or niobium atoms.

The present paper is organized as follows. In Sec. I, an introduction about the importance of the study developed in the present paper is given. In Sec. II, we present information on the preparation of the samples; besides, experimental details on the different techniques used to study Mg-based nanostructured films are specified. In particular, we give information concerning x-ray structural analysis and PAS techniques; that is, PALS and CDB. Section III is devoted to presenting and discussing the results obtained. This section is divided in subsections in which different issues are discussed: (i) H_2 desorption kinetics, (ii) Mg matrix structure and Nb aggregation, (iii) vacancylike defects and vacancy clusters studied using PAS (purposely, positron studies were addressed to the analysis of the vacancylike evolution by means of *ab initio* calculations and PALS and CDB), and (iv) mechanism of hydrogen desorption. Finally, in Sec. IV we give the main conclusion of the present work.

II. EXPERIMENTAL

A. Samples

Mg film samples with thickness $\sim$20 μm, were deposited by rf magnetron sputtering on graphite wafers using high-purity Ar as the working gas. The Nb doping was obtained with small Nb fragments lying on the Mg target.[11] The background pressure in the deposition chamber was in the low 10^{-5} Pa. The deposition process was carried out at 0.5 Pa Ar pressure and 150 W rf power without substrate heating. The target size was 10 cm in diameter while the target-to-substrate distance was 4 cm. These conditions resulted in a Mg growth rate of about 10 μm/h. Assuming that the residual vacuum in the deposition chamber at 10^{-5} Pa is composed of water, we estimated an oxygen contamination level of the Mg films in the 10^{-4} at.$^{-1}$. Samples were coated with a 15-nm-thick Pd capping layer without interrupting the vacuum conditions in the process chamber. The capping layer protects the film samples from surface oxidation and catalyzes the H_2 dissociation/recombination process during the H_2 sorption process. Series of films were prepared, with content of Nb $\sim$1 at. % (low Nb content) and with Nb $>$3 at. % (high Nb content). Measurements with energy dispersion spectroscopy (EDS) gave $\sim$1 at. % and $\sim$5 at. % Nb concentrations for the two series of samples measured by PAS and, $\sim$1 at. % and $\sim$3 at. % Nb concentrations for the two series of samples measured by EXAFS and XRD. The deposited samples spontaneously peeled off from the graphite substrate after exposure to air at ambient conditions.

The self-supporting Nb-doped Mg samples were then introduced in a Sievert-type apparatus[16] where their surface was activated by an annealing treatment at 573 K in a H_2 atmosphere at 0.8 MPa. Using these treatment parameters, during the activation procedure, the present samples absorb H_2 amounts under the detection limit of the Sievert system, indicating that the metal-to-hydride phase transformation has not occurred. Samples were considered activated as

soon as they start to absorb hydrogen. Successively, without interrupting the vacuum condition, the samples were submitted to H_2 sorption cycles at 623 K. Each sorption cycle consisted of two steps: (i) The sample was exposed to 1 MPa H_2 gas for 20 h to induce the H_2 absorption and then (ii) to vacuum to induce the H_2 desorption. In Mg-based samples the absorption step led to the Mg-to-MgH_2 phase transformation, while the desorption step led to the MgH_2-to-Mg phase transformation. The experimental setup permits the measure of the H_2 desorbed amount and the study of the H_2 desorption kinetics.[16]

Measurements were performed on the two series of Nb-doped samples. To identify the samples we have labeled them #LC and #HC for the series of samples with low and high Nb content, respectively. #0LC and #0HC indicate the as-deposited samples, while labels such as #nLC and #nHC represent samples submitted to n H_2 sorption cycles ($n = 1$ to 8) for samples of Mg doped with low and high Nb content, respectively. The undoped Mg samples are labeled as n#, where n is the number of cycles; 0# identifies the undoped Mg as-deposited sample.

CDB measurements were carried out also on a series of undoped Mg films treated as well as doped Nb-Mg films: activated by an annealing treatment at 573 K in a H_2 atmosphere at 0.8 MPa and submitted to H_2 sorption cycles at 623 K. PALS measurements on the same undoped Mg samples were presented and the results obtained were discussed in Ref. 14.

B. X-ray structural analyses

Structural information on the as-deposited samples and on the samples after desorption steps of successive H_2 sorption cycle, was obtained by XRD and EXAFS at the Nb K edge. XRD measurements were carried out by a Brucker D8 Advance diffractometer in a Bragg-Brentano geometry at 40 kV and 40 mA, using Cu K_α radiation. XRD measurements were used to evaluate the Mg grain size by the Debye-Scherrer analysis of the Mg (002) reflection peak. To investigate the aggregation state of Nb atoms, we have used EXAFS spectroscopy at the Nb K edge. The EXAFS measurements were performed at the Italian beamline GILDA of the European Synchrotron Radiation Facility (ESRF). The monochromator was equipped with two Si (311) crystals and to reject higher harmonics a couple of Pt-coated mirrors working at an incidence angle of 2.7 mrad were used. EXAFS spectra were collected in fluorescence mode by a 13-element high-purity Ge detector. Samples were cooled at 80 K to limit thermal vibrations. As standard reference, the spectrum of a Nb foil was also measured in transmission mode. Data analysis was based on the FEFF8-FEFFIT code.[7,22] For bcc Nb clusters, the first Nb coordination shell is split into two distances, R1 and R2, pertinent to two coordination numbers (CNs) CN1 and CN2: To fit the signal from bcc clusters, we have used the constraints CN2/CN1 = 6/8 and R2/R1 = 1.15, as in Nb bulk; the same Debye-Waller factor was attributed to the two subcoordinations. These constraints did not significantly alter the fitting results. Together with the signal from Nb clusters, a Nb-Mg correlation due to dispersed Nb atoms was considered, as well as a Nb-O signal to account for a minor dispersed fraction. In these conditions the degrees of freedom were 3–5.

It is worthy to remark that, as far as the Nb dopant is concerned, XRD is mainly sensitive to large Nb clusters, while EXAFS probes the average local site of all the Nb atoms, averaging the dispersed fraction as well.

C. PAS techniques

To identify vacancylike defects and to study their evolution as a function of the hydrogen sorption cycles, PALS, single-detector Doppler broadening DBS, and CDB were used. These techniques were applied using variable-energy slow positron beams.

Positrons injected in a solid with energy ranging from a few eV to some keV slow down in few picoseconds (1–3 ps at 300 K), reaching thermal energy with the material. For monoenergetic positrons, the stopping profile can be well described by a derivative of a Gaussian function.[23,24] The mean stopping depth $\langle z \rangle$ is related to the positron implantation energy E by the equation $\langle z \rangle = \frac{40}{\rho} E^{1.6}$ nm, where E is expressed in keV and the material density ρ in g cm^{-3} (1.74 g cm^{-3} for Mg).[24]

After thermalization, positrons start a diffusive motion, ending their life by annihilating with an electron into two 511-keV γ rays. A description of the slowing-down and diffusion processes can be found in Ref. 25. During the diffusion motion, a fraction of implanted positrons can reach the surface of the sample and annihilates in a surface state. This fraction decreases as the positron implantation energy increases. Another fraction of positrons annihilates in a bulk delocalized state and rises by increasing the positron implantation energy. If open-volume defects are present in the solid, a fraction of positrons is efficiently trapped into those sites due to the lack of a positive charge. Trapped positrons annihilate in a localized state with electrons present in the open-volume defects. Information on the type of defect can be obtained by analyzing the 511-keV annihilation peak spectra (specifically, DBS) and the positron lifetime spectra (see Ref. 26). Details about the atoms surrounding or decorating the open-volume defects can be obtained from CDB by studying the positron annihilation with high-momentum electrons (see Ref. 26).

In PALS a start signal, corresponding to the positron injection in the sample, and a stop signal at positron annihilation time are required for lifetime measurements. In the positron lifetime spectra, various positron states appear as different exponential decays,

$$F(t) = \sum_i^N \frac{I_i}{\tau_i} \exp\left(-\frac{t}{\tau_i}\right). \quad (1)$$

The number of positron lifetimes τ_i and their associated intensities I_i can be obtained by means of the PATFIT package.[27] The mean lifetime is given by $\bar{\tau} = \sum_i I_i \tau_i$. The positron lifetime is a measure of the electron density sampled by the positron at the annihilation site; therefore, larger open volumes are characterized by longer lifetimes (the local electron density decreases).

PALS measurements were carried out with the PLEPS (Pulsed Low Energy Positron Beam) apparatus[28] at the high intense positron source NEPOMUC (Neutron Induced

Positron Source Munich).[29] In this system, the start signal is given by the pulsing of the beam and the stop signal by the 511-keV γ rays detected with a BaF_2 detector. The overall (detector plus pulsing system) time resolution was 280 ps. Lifetime spectra $F(t)$ in the bulk of Mg films were acquired with a positron implantation energy E higher than 12 keV, up to 18 keV, which is the maximum energy allowed at PLEPS. In Mg, in this energy range, the mean positron implantation depth ranges from 1.2 to 2.4 μm.

In the Doppler broadening spectroscopies, the Doppler shift ΔE_γ of the 511-keV annihilation γ radiation caused by the motion of the positron-electron annihilating pair is studied. The Doppler shift is related to the longitudinal momentum component of the positron-electron pair p_L by $\Delta E_\gamma = 1/2cp_L$. The Doppler shift ΔE_γ gives rise to the broadening of the 511-keV annihilation line $G(E,E_\gamma)$, where E is the positron implantation energy and E_γ is the energy of the γ rays. The $G(E,E_\gamma)$ line shape is the one-dimensional momentum distribution of the positron-electron pair convoluted with the apparatus resolution function and it is usually characterized by shape parameters. In this work, we have used the low electron-momentum parameter S defined as the ratio of the counts in the central region of the annihilation line $G(E,E_\gamma)$ to the total counts in the line. Positron annihilations into open-volume defects reflect in an increase of the S parameter due to the lack of core electrons. Conversely, annihilation with core electrons contributes to the high momentum region of the $G(E,E_\gamma)$ line (the wing of the annihilation line). Indeed, the wave function of trapped positrons in open-volume defects slightly overlaps with the core or outermost core electrons of the surrounding atoms. Since these annihilations are very few, to study the high-momentum region the more resolved CDB technique, in which the background is strongly reduced, was used.[30–32]

DBS and CDB measurements were performed with a continuous slow positron beam at the Trento University.[33,34] The beam was tunable in the 0.05–25 keV energy range and the annihilation γ rays were detected with two high-purity germanium (HPGe) detectors, 45% efficiency, 1.4 keV resolution at 511 keV, in a 180° configuration. Annihilation spectra, for the evaluation of the S parameters, were acquired using a microspectra method stabilized by a software procedure.[35] This method makes it possible to evaluate the energy calibration for each acquired spectrum. To calculate the S parameter, the energy windows were chosen as $|511 - E_\gamma| \leqslant 0.85$ keV and $|511 - E_\gamma| \leqslant 4.25$ keV for the central and the total area of $G(E,E_\gamma)$ spectra, respectively. The S parameters were measured with a statistical error of 0.1% (more than 2.5×10^5 counts in each annihilation spectrum) and normalized to the S value of Mg bulk ($S_{\mathrm{Mg}} = 0.586$).

By means of CDB, we studied the high momentum region of $G(E,E_\gamma)$ spectra corresponding to momenta in the range of $5 \times 10^{-3}\ m_o c \leqslant p_L \leqslant 30 \times 10^{-3}\ m_o c$. Here, m_o is the electron rest mass. Positron annihilation with core electrons is a fingerprint of the chemical elements and gives information on the decoration of open-volume defects.[30–32] The information about the environment around the defects mentioned is highlighted by a peak or a valley in the ratio curves constructed as the ratio between $G(E,E_\gamma)$ and a reference $G_{\mathrm{Mg}}(E_\gamma)$ spectrum measured in a undefected Mg sample.

$G(E,E_\gamma)$ is a linear combination of the CDB characteristic curves describing positron annihilation in the different states of the material, for example, annihilation into vacancies, vacancy clusters, and annihilation with Nb electrons. Knowing the CDB characteristic curves, from a fitting analysis of the $G(E,E_\gamma)$ curves, the fraction of positrons annihilating in the different states of the material can be obtained.

Evaluation of the characteristic CDB momentum distribution curves and of the reference lifetime values, needed for the interpretation of the results presented in this work, were obtained by means of measurements on selected samples.

1. *Reference measurements for PALS*

The reference lifetime value for positrons annihilations in Mg bulk was measured in well-annealed Mg (0001) single crystals (99.99% purity). The positron Mg bulk lifetime was found to be 218 ± 2 ps. To obtain the value of the lifetime in monovacancies we measured deformed Mg. Following ideas of Hautojarvi *et al.*,[36] high-purity Mg polycrystalline samples were deformed by compression mechanical tests at room temperature (RT) for different deformation levels up to 50%. From the analysis of PALS spectra obtained at RT, a signal coming from vacancylike defects could not be detected. Conversely, following the procedure proposed by Somoza *et al.*,[37] a Mg single crystal was severely deformed by cold working at RT and clear evidence on the presence of monovacancies still at RT was obtained. Specifically, in PALS spectra a strong lifetime component of 245 ± 5 ps was observed. This lifetime value is in very good agreement with those previously reported by Hautojarvi *et al.*[36] and Folegati *et al.*[38] The existence of monovacancies in Mg at RT was also confirmed by CDB measurements.[37,39]

2. *Reference measurements for CDB*

The reference CDB momentum distribution for pure Mg $G_{\mathrm{Mg}}(E_\gamma)$ was obtained by measuring the bulk of a Mg single crystal previously submitted to an annealing treatment in vacuum at 500 °C. To obtain the pure Nb reference curve $G_{\mathrm{Nb}}(E_\gamma)$, a pure Nb single crystal (99.95% purity) was measured. Furthermore, the corresponding CDB curve of magnesium oxide $G_{\mathrm{MgO}}(E_\gamma)$ was obtained from measurements at the surface of a Mg single crystal. This distribution was considered representative of the positron annihilation with electrons of oxygen atoms bound to Mg.

In this work, all the CDB curves will be presented as a function of the momentum p_L in the form of difference of momentum distributions relative to the $G_{\mathrm{Mg}}(E_\gamma)$ curve obtained measuring the well-annealed pure Mg, according to the following expression:[40]

$$G_i^o = \frac{G_i(E_\gamma) - G_{\mathrm{Mg}}(E_\gamma)}{G_{\mathrm{Mg}}(E_\gamma)}, \tag{2}$$

where i indicates positron annihilation in the state i: Nb and Mg single crystal, MgO, vacancies in Mg (v-Mg), vacancy clusters in Mg (vc-Mg).

In Fig. 1, G_{Nb}^o is characterized by a strong peak centered at about $11.8 \times 10^{-3}\ m_o c$. In the G_{MgO}^o distribution, positron annihilations with high-momentum electrons of oxygen appear with a broad peak centered at about $11.3 \times 10^{-3}\ m_o c$. For

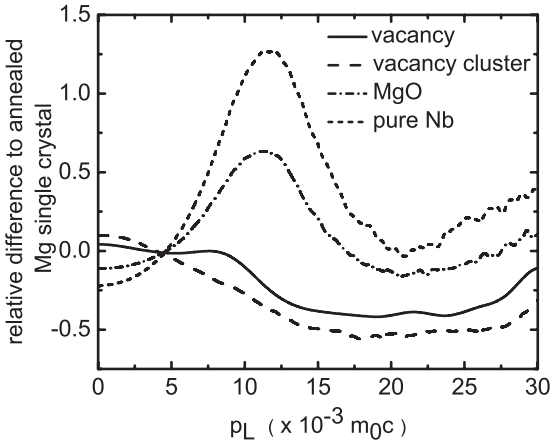

FIG. 1. Characteristic momentum distribution CDB ratio curves for positrons annihilating in niobium bulk, in oxygen-rich sites, and in open volume defects in Mg: vacancy and vacancy clusters. The ratio curves are presented as a relative difference with respect to a curve obtained for an annealed Mg single crystal [see Eq. (2)].

$p_L > 18 \times 10^{-3}\ m_o c$ the data of G_i^o curves were smoothed using the moving average method, specifically a seven points adjacent averaging.

The characteristic curve of a monovacancy $G^o_{v-\mathrm{Mg}}$ was obtained from the CDB curves corresponding to the deformed Mg single crystal. In Fig. 1, the broad maximum at $p_L = 0$ in the $G^o_{v-\mathrm{Mg}}$ curve comes from positron annihilations with low momentum electrons into the vacancy, while the bump around $8 \times 10^{-3}\ m_o c$ could be attributed to positron quantum confining in the vacancy. This effect was widely discussed for vacancies in Al.[41]

To obtain the characteristic curve of vacancy clusters in Mg $G^o_{vc-\mathrm{Mg}}$, the surface of Mg foils 0.5 μm thick was mechanically polished and then annealed. In Fig. 2, the S versus E curve, as measured in the polished sample, is shown. Normalized S values increase up to a depth of about 100 nm, pointing out the presence of vacancylike defects. Afterward, one Mg foil was annealed for 1 h at 420 °C ten times while another sample was treated for 10 h at 420 °C, under a 1 bar CO_2 atmosphere.[42] Since both $S(E)$ curves of the two annealed samples were practically superimposed, within the error bars, in Fig. 2 only the curve for the sample annealed for 10 h is reported. Annealing promotes vacancy clustering, as clearly indicated by the significant increase of S values around a depth of 100 nm. Vacancy clusters were then removed applying, to the previous annealed samples, a further annealing at 500 °C for 1 h: The corresponding $S(E)$ curve (see Fig. 2) shows the monotonically increase from the S surface value to that of Mg bulk, typical of a free-defected Mg.

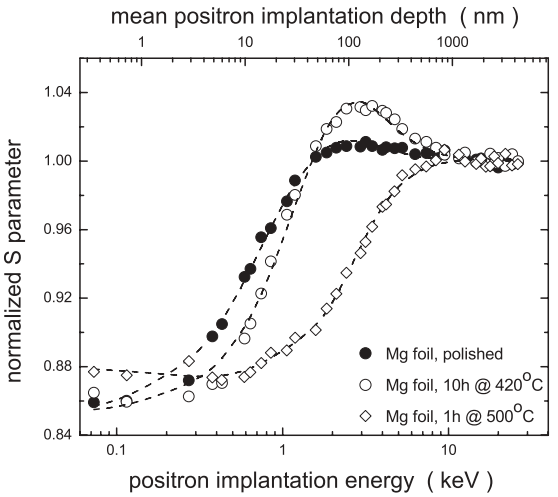

FIG. 2. Normalized S parameter as a function of the positron implantation energy (lower scale) and of the mean positron implantation depth (upper scale). S curves correspond to polished Mg foils and to foils annealed for 10 h at 420 °C and foils submitted to the same heat treatment followed by an annealing for 1 h at 500 °C.

The $S(E)$ curve is a linear combination of characteristic S values multiplied by the fraction $f(E)$ of positrons annihilating at the MgO surface $[S_{\mathrm{MgO}}, f_{\mathrm{MgO}}(E)]$, in the Mg bulk $[S_{\mathrm{Mg}}, f_{\mathrm{Mg}}(E)]$ and in the different j defect states $[S_{dj}, f_{dj}(E)]$:

$$S(E) = S_{\mathrm{MgO}} f_{\mathrm{MgO}}(E) + S_{\mathrm{Mg}} f_{\mathrm{Mg}}(E) + \sum_j S_{dj} f_{dj}(E), \quad (3)$$

with

$$f_{\mathrm{MgO}}(E) + f_{\mathrm{Mg}}(E) + \sum_j f_{dj}(E) = 1 \quad \forall E. \quad (4)$$

The characteristic S values and the fraction $f(E)$ of positrons annihilating in the different states is extracted by fitting the $S(E)$ curves with the stationary positron diffusion equation model; for details see Refs. 35 and 43. As an example, the curves of the fraction $f(E)$ as obtained by the diffusion model for the sample annealed 10 h at 420 °C are shown in Fig. 3. From this figure, the high positron fraction annihilating into vacancy clusters (labeled defect #1 in the figure) for a mean positron implantation depth around 100 nm can be seen.

In Fig. 2, dashed lines through the experimental points are the best fit to the $S(E)$ data using the diffusion model.

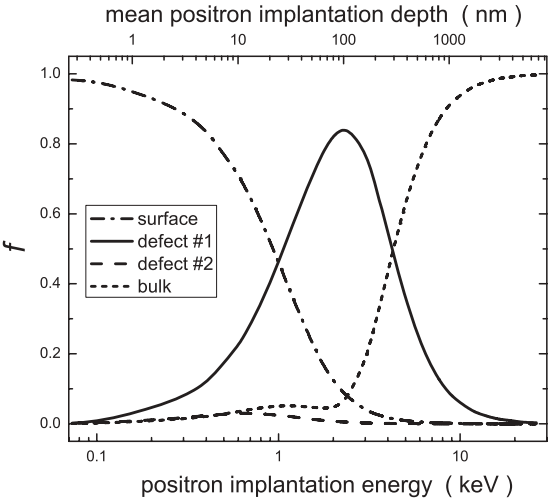

FIG. 3. Fractions of positron annihilated into the different states as a function of the positron implantation energy (lower scale) and of the mean positron implantation depth (upper scale). Values of the parameter f were obtained by fitting with the positron stationary diffusion equation the experimental $S(E)$ values as measured in pure Mg foil annealed at 420 °C (see Fig. 2). Defect #1: vacancy clusters (see text).

In the polished foil the defects centered at about 100 nm depth were characterized by a characteristic value $S_{d1}/S_{\mathrm{Mg}} = 1.022$. This low S_{d1} value can be associated with vacancylike defects. After annealing, a very high value of $S_{d1}/S_{\mathrm{Mg}} = 1.052$ due to vacancy clusters was found. A small fraction of positrons annihilates in a second kind of defects located very near the surface and which is characterized by $S_{d2}/S_{\mathrm{Mg}} = 0.906$ (see bold dashed line in Fig. 3).

When all defects are removed, by fitting the $S(E)$ curve of the free-defected sample a positron diffusion length of about 70 nm was obtained.

The characteristic curve of vacancy clusters $G^{o}_{vc-\mathrm{Mg}}$ was extracted from CDB spectra $G(E,E_\gamma)$ measured at selected energies E on the foils annealed at 420 °C. To this aim, we have followed the procedure reported in Refs. 34, 44–46.

The $G(E,E_\gamma)$ spectra, like the $S(E)$ curves [see (3) and (4)], are linear combination of the characteristic spectra $G_i(E_\gamma)$ for the different states i (i.e., MgO, Mg, and defects labeled dj) multiplied by the fraction f(E) of positrons annihilating at the MgO surface, in the Mg bulk, and in the different j defected states:

$$G(E,E_\gamma) = G_{\mathrm{MgO}}(E_\gamma) f_{\mathrm{MgO}}(E) + G_{\mathrm{Mg}}(E_\gamma) f_{\mathrm{Mg}}(E) + \sum_j G_{dj}(E_\gamma) f_{dj}(E). \quad (5)$$

Coincidence Doppler broadening momentum distributions $G(E,E_\gamma)$ were measured at four selected positron implantation energies and knowing the $f_{\mathrm{MgO}}(E), f_{\mathrm{Mg}}(E), f_{dj}(E)$ values, the curves $G_i(E_\gamma)$ were obtained by solving system of equations (5) and the G^{o}_{i} calculated with (2).

The calculated $G^{o}_{vc-\mathrm{Mg}}$ is also shown in Fig. 1. For this momentum distribution, the maximum at $p_L = 0$ is higher than that of the characteristic curve for positron annihilating in monovacancies $G^{o}_{v-\mathrm{Mg}}$. This behavior is due to the increased positron annihilation with lower momentum electrons in the vacancy clusters. The valley above $5 \times 10^{-3}\, m_0 c$, is attributed to a lower overlapping of the positron wave function with the Mg atoms surrounding the vacancy clusters. The $G^{o}_{vc-\mathrm{Mg}}$ distribution shown in Fig. 1 is considered a fingerprint of vacancy clusters. The different size of vacancy clusters could change the intensity of the peak and of the valley but not the general shape.[47]

The extracted $G_{\mathrm{Mg}}(E_\gamma)$ and $G_{\mathrm{MgO}}(E_\gamma)$ characteristic curves were found to be consistent with the corresponding curves measured in the bulk and at the surface of the Mg single crystal.

III. RESULTS AND DISCUSSION

A. H_2 desorption kinetics

Conversely to the process observed in pure Mg samples,[14] the Nb-doped Mg samples require only few H_2 sorption cycles to be completely hydrogenated. In the 2nd cycle, the #LC and #HC samples absorb, in fact, a hydrogen amount equivalent to about 50% and 70%, respectively, of the nominal capacity of Mg.

In Fig. 4 selected desorption curves for #LC and #HC series are presented in order to show the trend of the H_2 desorption kinetics. In this figure, experimental data were normalized to the nominal H_2 absorption capacity of Mg. The curves show the transformed fraction of the hydride samples as a function of time. In the figure, experimental data are represented by symbols while the solid lines represent fitting curves obtained as discussed below.

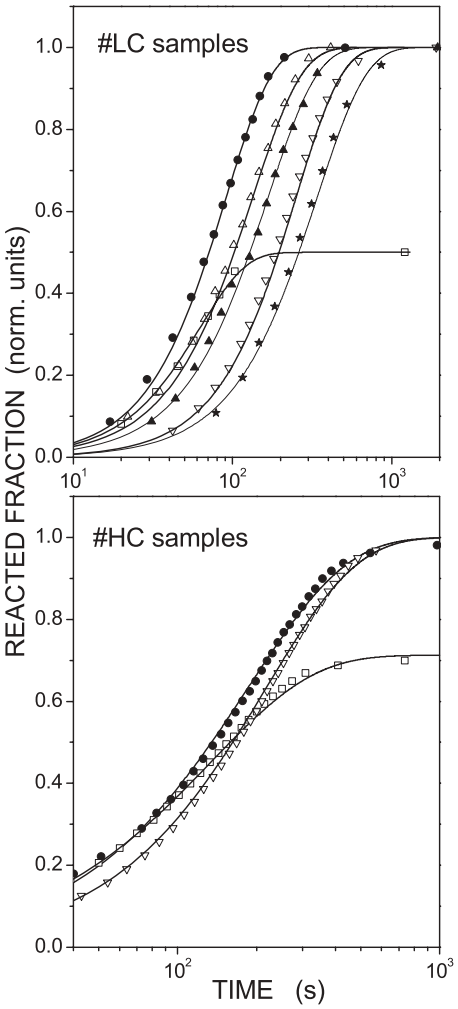

FIG. 4. Selected H_2 desorption curves for the #LC (top panel) and #HC (bottom panel; Nb content ~3 at. %) Nb-doped Mg samples: reacted fraction of the hydride samples as a function of time. In the top panel, the desorption curves obtained for the 2nd (open squares), 3rd (solid circles), 5th (open up triangles), 6th (solid up triangles), 9th (open down triangles), and 12th (solid stars) sorption cycles are shown. In the bottom panel, the desorption curves corresponding to the 2nd (open squares), 3rd (solid circles), and 9th (open down triangle) sorption cycles are represented.

The top panel of Fig. 4 shows the desorption curves corresponding to the #LC samples: The 2nd desorption cycle data are reported using open squares; then, from left to right, the curves representing the 3rd, 5th, 6th, 9th, and 12th sorption cycles are shown. Stationary conditions were reached with the 12th cycle. In the bottom panel, desorption curves obtained for the #HC samples are presented. Specifically, the desorption curves of the 2nd, 3rd, and 9th sorption cycles are shown. For the 9th cycle, stationary conditions were reached.

From Fig. 4 relevant information can be obtained. In both kinds of samples, the H_2 desorption kinetics becomes slower

after successive cycles until reaching the stationary condition. This effect is more marked in the #LC samples in whch 10–12 sorption cycles are necessary to attain the sorption stationary condition. In the #HC samples, to reach the same sorption condition only 3–4 cycles are needed, as observed in samples with Nb content of ∼3 and ∼5 at. %. The velocity of the H_2 desorption process can be qualitatively described by the typical desorption time $\tau_{\frac{1}{2}}$ defined as the interval time needed to transform half of the MgH_2 into Mg. When the H_2 adsorbed amount is close to the nominal Mg capacity, $\tau_{\frac{1}{2}}$ increases from ∼60 s (3rd cycle) to ∼240 s (stationary condition) in the #LC sample and from ∼120 s (3rd cycle) to ∼160 s (stationary condition) in the #HC sample.

The hydrogen desorption from magnesium hydrides generally occurs by the nucleation and growth (NG) mechanism. The Mg nucleation starts at special nucleation sites in the parent hydride phase and its growth can be interface limited (it is controlled by the rate of dissociation of the hydride at the metal-hydride interface) or diffusion limited (it is controlled by the long-range diffusion of H atoms to the sample surface). When the hydride-to-metal phase transformation is controlled by surface processes, such as the H molecular recombination and H_2 release, the hydrogen desorption curves can be reproduced by using the linear equations $\alpha = kt$, where α is the transformed fraction of the sample at a time t ($t = 0$ corresponds to the beginning of the process) and k the rate constant.[48] This equation does not clearly fit the experimental data in Fig. 4 and, consequently, it can be safely excluded that in the samples studied in the present work the recombinative desorption of H atoms at the Pd-coated surface is the rate-limiting step in the H_2 desorption kinetics.

The desorption curves in Fig. 4 have a sigmoidal shape and their best fits were obtained by using the Johnson-Mehl-Avrami (JMA) equation $\alpha(t) = 1 - \exp[-(kt)^n]$. This equation describes the kinetics of the phase transformations when the rate-limiting step is given by the NG process of the Mg phase in the parent MgH_2 phase.[49] In this equation $\alpha(t)$ is the fraction of transformed material, $k = k(T)$ is the rate constant, and n is the reaction order. The JMA equation well fits the experimental data reported in Fig. 4. The fit indicates that in the #LC samples the H_2 desorption kinetics at 623 K occurs with a $n = 1.5$ reaction order, when the number of cycles increases the value of the rate constant k decreases from 1.6×10^{-2} to 2.9×10^{-3} s^{-1}. In the #HC samples, the reaction order is $n = 1$ and the value of the rate constant k decreases from 7.5×10^{-3} to 4.0×10^{-3} s^{-1}. In particular, after reaching stationary conditions, desorption analysis at temperatures from 583 K to 623 K indicated that the desorption process still obeys a NG mechanism with a reaction order $n = 1.5$ and an activation energy of 78 ± 5 kJ/mol for the #LC samples,[12] and a reaction order $n = 1$ and an activation energy of 51 ± 5 kJ/mol for the #HC samples.[13] Note that in pure Mg samples, a reaction order $n = 4$ and an activation energy of 140 ± 5 kJ/mol were reported.[13]

The variation of the velocity of the H_2 sorption process occurring after successive H_2 sorption cycles can be thus related to changes in the structure of the Mg matrix at nanoscale level that influence the mechanism of the Mg nucleation and growth.

B. Mg matrix structure and Nb aggregation

Scanning electron microscopy (SEM) measurements on the cross section of the sample have shown that the films grow with a columnar structure: The typical size of the columns is 0.4–0.5 μm while the height of the columns is comparable with the film thickness.

The evolution of the crystalline phase involving the Mg matrix was studied by XRD. In the as-deposited samples, both #0LC and #0HC, Mg layers grow in the (0002) orientation and they maintain this orientation after successive H_2 sorption cycles. In the 1st H_2 sorption cycles, the Pd capping film forms a bimetallic crystalline compound with Mg (Mg_6Pd). Furthermore, in the as-deposited samples no XRD signal attributable to Nb-related crystalline phase was detected. The Mg-Nb phase diagram shows a wide immiscibility interval, as a function of the concentration, of the Mg and Nb atoms due to their different atomic sizes, electronegativity, and crystalline structure in the condensed phase. The H_2 cycling promotes the Nb precipitation in the Mg matrix.

In Fig. 5, the XRD spectra of the #LC samples after the 2nd and 4th cycles are shown. This figure indicates that in these samples the formation of large bcc Nb nanocrystals (size ∼10 nm) occurs only after the 4th cycles. Conversely, in the #HC samples the presence of large bcc Nb nanocrystals or of Nb nanocrystals, with expanded lattice parameter having similar size, is evident after the 1st cycle. The Nb lattice expansion was previously attributed to $NbH_{0.89}$ clusters.[12,50] Note that by the XRD analysis no information can be retrieved from amorphous structure, from small aggregates consisting of few atoms and from the fraction of dispersed Nb atoms.

By the Debye-Scherrer equation applied to the (0002) Mg reflection peak, the grain size was found to remain almost constant after successive H_2 cycles in the #LC series (∼80–90 nm), as in pure Mg samples (∼100–120 nm).[14] Differently, a grain size reduction was observed in the #HC series: The size of the Mg grain was ∼90 nm in the as-deposited sample,

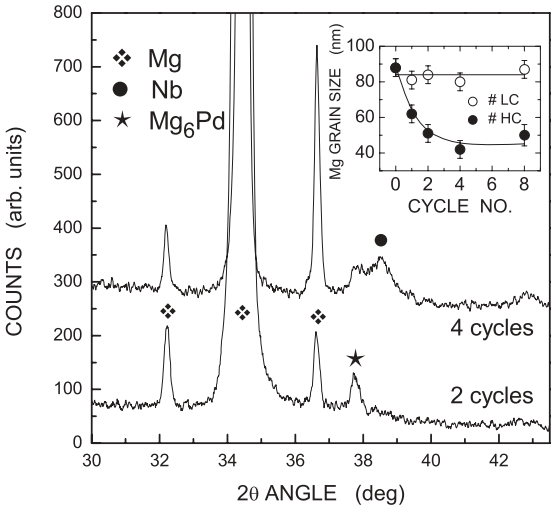

FIG. 5. XRD spectra of the #LC sample after the 2nd and 4th H_2 sorption cycles at $T = 623$ K. In the inset, we report the Mg grain size as evaluated by Debye-Scherrer analysis of the Mg (002) peak for the #HC and #LC samples after successive H_2 sorption cycles.

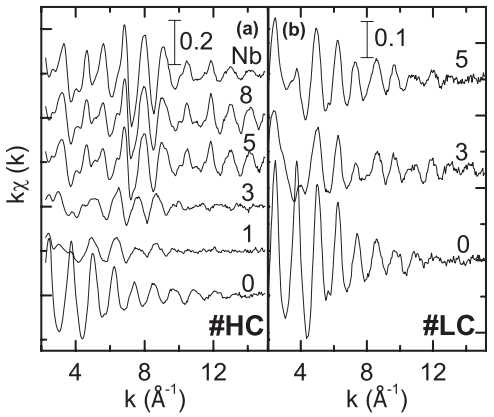

FIG. 6. k-weighted EXAFS spectra at the Nb- edge for the #HC and #LC samples after successive H_2 sorption cycles. The cycle number is indicated; the spectrum of Nb metal (divided by 4) is reported for comparison in (a).

~60 nm in the 1st cycle, and 40–50 nm in the successive cycles. See the inset in Fig. 5.

The EXAFS spectra of the #HC and #LC samples are shown in Fig 6: Spectra are pertinent to the as-deposited samples and to samples submitted to successive H_2 sorption cycles (1 to 8). The figure shows that the spectrum of the as-deposited doped Mg samples changes upon successive H_2 sorption cycles and becomes progressively similar (after 5 and 8 cycles) to that of metallic Nb. This evolution is more evident in the #HC samples, thus suggesting that the aggregation process is slower in the #LC samples. In Figs. 7(a) and 7(b) the corresponding Fourier transform moduli and the fits are shown. In both samples a main peak centered at about 2.7 Å and mainly due to Nb-Mg correlations can be seen. In the #HC samples the couple of peaks typical of bcc Nb phase are well evident from the 5th cycle on, while in the #LC samples case the first shell peak never splits into two ones. The results of the fitting procedures are reported in Table I; the fit superimposed to the experimental filtered data (k space) is also reported in Figs. 7(c) and 7(d) for two representative cases, together with the contributions from the single scattering coordination.

Consider first the #HC samples. The results on the as-deposited film indicate that, while most of the additive is atomically dispersed and bonded to the Mg matrix (the Nb-Mg coordination is the main signal), a fraction of Nb atoms forms small aggregates. We observe that the Nb-Nb correlation is not split into the two typical distances of the bulk bcc phase and that the Nb-Nb distance is shorter than that in the bulk (see Table I). These two features indicate that these Nb metal aggregates are very small. In fact, small TM clusters exhibit a contraction of the nearest neighbor distance with respect to the bulk phase.[51–53] For small Nb clusters, experimental structural data are lacking; the available calculations indicate that clusters of 7–11 atoms (i.e., subnanometer sized) exhibit an average nearest-neighbor distance of 2.60–2.65 Å,[54–58] suggesting that, in our case, the average size of the small Nb aggregates is slightly larger, likely in the ~1-nm range. This is compatible with the results of XRD analysis that for this sample did not detect any Nb crystalline phase, owing to their small size. As a comparison, tight binding simulations indicate the bcc as the

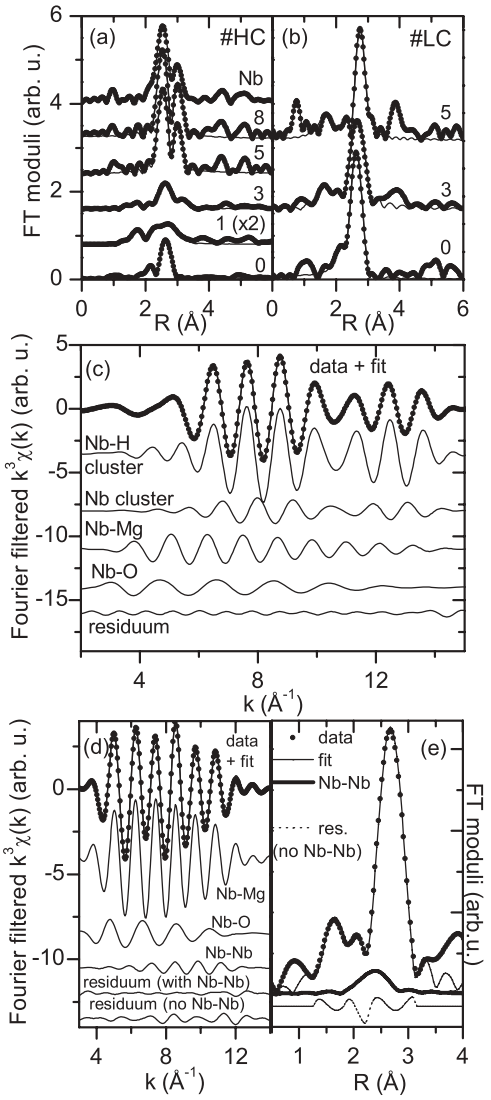

FIG. 7. (a),(b) k^3-weighted Fourier transform moduli (markers) and relative fits (line, fitting range $R = 1.2$–3.4 Å) for the #HC (a) and #LC (b) samples; the corresponding signal from metallic Nb is reported in (a). (c),(d) Fourier filtered signal in the fitting range and corresponding fit for two representative cases after 3 cycles: #HC (c) and #LC (d) samples; the single scattering contribution to the signal is shown together with the residuum; in (d) the residuum without the Nb-Nb contribution is also reported. (e) Zoom in the fitting range for the spectrum in (b) for the #LC sample after 3 cycles, superimposed to the best fit curve; the contribution from Nb-Nb coordination is shown.

most stable structure for Nb clusters larger than about 1.5 nm (~100 atoms),[59] and experiments show that nanostructured Nb with a grain size of 4–5 nm exhibits a well-visible bcc crystalline structure.[60]

The 1st H_2 cycle of the #HC layers, promotes a strong rearrangement of the Nb site: The Nb-Mg correlation drops down (the coordination number of the Mg shell is ~1/3 of that in the as-deposited layer) and a further formation of Nb aggregates occurs, characterized by a splitting of the Nb-Nb first shell distance as expected from the bcc phase. Almost the same picture occurs after the 3rd H_2 cycle where

TABLE I. Results of the EXAFS analysis on Nb-doped Mg film samples after successive H_2 sorption cycles. CN is the coordination number (the backscatterer atomic species is reported), R the interatomic distance, and σ^2 the Debye-Waller factor. Crystallographic data for the bcc metal and for the α-$NbH_{0.9}$ phase are reported for comparison.[53]

Sample	Atom	CN	R (Å)	σ^2 ($\times 10^{-4}$ Å)
		Nb-doped Mg samples with high Nb content		
#0HC	Mg	8.5 ± 0.3	3.08 ± 0.01	72 ± 4
	Nb	0.8 ± 0.2	2.74 ± 0.01	51 ± 10
#1HC	O	0.7 ± 0.1	2.12 ± 0.01	39 ± 12
	Mg	2.8 ± 0.4	3.13 ± 0.01	57 ± 14
	Nb[a]	1.1; 0.8 ± 0.3	2.86; 3.30 ± 0.02	74 ± 22
	Nb[b]	1.5; 1.1 ± 0.4	2.98; 3.43 ± 0.02	74 ± 22
#3HC	O	1.0 ± 0.3	2.09 ± 0.02	75 ± 23
	Mg	1.9 ± 0.4	3.08 ± 0.02	52 ± 18
	Nb[a]	0.5; 0.4 ± 0.2	2.84; 3.28 ± 0.03	56 ± 13
	Nb[b]	2.2; 1.7 ± 0.5	2.97; 3.42 ± 0.01	56 ± 13
#5HC	Nb	3.2; 2.4 ± 0.2	2.86; 3.31 ± 0.01	32 ± 3
#8HC	Nb	3.6; 2.7 ± 0.2	2.86; 3.31 ± 0.01	32 ± 3
		Nb-doped Mg samples with low Nb content		
#0LC	Mg	9.0 ± 0.3	3.09 ± 0.01	71 ± 3
	Nb	0.4 ± 0.1	2.72 ± 0.01	51 ± 10
#3LC	O	1.5 ± 0.7	2.08 ± 0.02	96 ± 47
	Mg	4.8 ± 0.5	3.11 ± 0.01	33 ± 8
	Nb	0.20 ± 0.08	2.70 ± 0.03	51 ± 10
#5LC	O	1.5 ± 0.7	2.14 ± 0.04	87 ± 45
	Mg	2.9 ± 1.0	3.15 ± 0.05	32 ± 3
	Nb[a]	0.7; 0.5 ± 0.3	2.86; 3.31 ± 0.02	42 ± 14
	Nb	1.7 ± 0.7	3.04 ± 0.02	43 ± 14
Nb	Nb	8; 6	2.86; 3.31	
$NbH^{0.9}$	Nb	8; 6	3.00; 3.45	

[a]Nb metal clusters.
[b]Hydrogenated Nb clusters.

the Nb-Mg coordination distances further decrease. If we consider the subject points discussed about the as-deposited sample, the splitting of the Nb-Nb coordination into two distances indicates that the cluster size is larger than that in the as-deposited film. We note that the Nb-Nb signal includes multiple contributions from both relaxed bcc clusters (same coordination distances as Nb bulk) and bcc clusters with longer (by about 4.5%) coordination distances. This second contribution is likely due to Nb clusters that absorbed hydrogen with a consequent expansion of the interatomic distances: The measured values are very close to the corresponding values in the Nb-H phase with H/Nb $\geqslant$ 0.8 and in the orthorhombic $NbH_{0.89}$ phase.[61] A fitting based on a simple model (with only Nb or a Nb-H phase in addition to the Nb-Mg coordination) does not reproduce our EXAFS data. The presence of H atoms in the Nb clusters in the desorbed sample is reasonably due to H atoms trapped in the Nb aggregates during the H_2 desorption process. After one or 2 cycles XRD detected the formation of either Nb or $NbH_{0.89}$ nanocrystalline phases,[12,50] which is related to the fact that XRD is mostly sensitive to the fraction of largest nanostructures. Anyway, the asymmetry of the measured diffraction peak strongly suggests the presence of a population of significantly smaller clusters of the other phase,[50] as shown by the EXAFS results. To this respect, the copresence of Nb-H and Nb nanophases in Mg matrix gives rise to a complex diffraction pattern where broad peaks are superimposed.[50] It is worth noting that both metallic and Nb hydride can coexist at room temperature, according to the Nb-H phase diagram.[62] In the EXAFS signal a Nb-O coordination is also present (visible in the region R ~1.8 Å in Fig 7(a), indicating that a minor part of Nb is oxidized (see Table I): This oxidation is probably due to Nb bonding with oxygen contaminants of the residual vacuum in the deposition chamber.

After the 5th and 8th cycles the Nb-Nb signal from the bcc relaxed clusters dominates the EXAFS spectrum, and the results after the 8th cycle are very similar to those obtained studying a fully activated sample doped with 5 at. % Nb:[7] XRD analysis showed here the formation of ~15-nm bcc Nb clusters. The low coordination number of the Nb shell could be likely due to both the presence of a fraction of Nb atoms still dispersed into the matrix and to a large population of relatively small bcc clusters. For this reason, it is worth pointing out that the large Nb clusters that dominate the XRD spectrum[7,50] (~10 nm diameter according to Debye-Scherrer analysis) involve likely only a fraction of the overall Nb population. As an example, considering a 6-nm-diameter bcc Nb cluster it contains about 6200 atoms of which about 30% are located in the surface region (defined as the spherical shell containing all Nb atoms whose distance from the surface is less than the first shell radius). Here, the average first shell coordination number is only about 15% lower than the

corresponding bulk value. This means that if all Nb atoms are aggregated in clusters of at least 6 nm, the measured coordination number would be essentially in agreement with the bulk value within the experimental uncertainty, which is definitely not the case. EXAFS results indicate that under this hypothesis (i.e., absence of small clusters) the dispersed Nb fraction, as estimated by the reduction of the coordination number for the Nb shell with respect to the bulk value, should be about 60% (upper limit). Conversely, if the large majority of clusters are very small (i.e., an ∼2-nm bcc cluster has $CN_1 \sim 5$), then the dispersed fraction could be about 30%–40%. Stress induced by repeated cluster structural expansion and relaxation during the absorption and desorption steps of each cycle[7] can likely induce a cluster fragmentation with a consequent significant dispersed Nb fraction. The EXAFS exclude a significant chemical bond between Nb and the matrix (Nb-Mg coordination is undetectable in the #HC film from the 5th cycle on), indicating that certainly after few cycles the site of Nb dispersed in the Mg matrix is not substitutional.

The EXAFS results from the #LC samples [see Table I and Figs. 7(b), 7(d), and 7(e)] indicate that the Nb clusterization process is slower. The as-deposited layer contains a small fraction of small Nb aggregates whose size is likely smaller than that of the #HC sample, as suggested by the shorter Nb-Nb distance (see Table I). Contrary to that observed for the high-concentration case, after 3 cycles the signal from bcc-like Nb clusters (first, the Nb shell split into two distances) is absent, indicating that in this case the Nb aggregation process is delayed. After 3 cycles, only one single Nb-Nb correlation signal is present: Even if this signal is small, it is nevertheless statistically significant, according to the F test[63] [see also the fitting residuum with and without the Nb-Nb contribution presented in Fig. 7(d), as well as its contribution to the total signal in the R space in Fig. 7(e)]. The presence of bcc Nb clusters (first, the Nb shell split into two distances) occurs only after 5 cycles, as shown from the EXAFS results in Table I. Correspondingly, in the XRD patterns (see Fig. 5) the signal from the Nb bcc is only slightly visible from the 4th cycle on. The last consideration is on the long Nb-Nb coordination that is observed at low concentration from the 5th cycle on: The Nb-Nb distance (3.04 Å) is similar to the one in crystalline NbO (where each Nb atom coordinates 6 O atoms at a distance of 2.10 Å and 12 Nb atoms at 2.98 Å). This coordination could be pertinent to an oxide phase that extends beyond the first Nb-O coordination and that, together with the Nb cluster growth, could contribute to modify the kinetics; work is in progress to investigate this point.

The present structural analysis on the as-deposited samples indicates that during the deposition process sputtered Nb atoms already form small Nb aggregates in the Mg matrix. The further precipitation of the Nb atoms in the supersaturated Mg matrix after deposition occurs via heterogeneous nucleation of the Nb atoms in preferential sites, typically extended defects of the host crystalline matrix (grain boundaries). In the first few H_2 cycles, a significant fraction of Nb is dispersed into the matrix and connected to Mg atoms. At this time, the aggregation process is mostly controlled by the atomic diffusion of the dispersed Nb fraction[64]: A lower Nb concentration delays the dopant aggregation in large nanoclusters (as seen from EXAFS and XRD results), thus favoring the formation of the small Nb aggregates. When upon cycling, the fraction of Nb connected to the Mg matrix significantly decreases and bcc Nb nanoclusters form (after the 1st H_2 cycle in the #HC samples and after the 4th cycle in the #LC ones), the cluster growth is controlled by the Gibbs-Thomson effect: Since the chemical potential is inversely proportional to the particle size, Nb atoms in the small aggregates migrate toward the larger bcc clusters. Consequently, Nb clusters continue growing while the smaller aggregates dissolve.[64,65]

C. Vacancylike defects and vacancy clusters

1. Ab initio calculations of positron lifetimes

In Nb-doped Mg samples, the presence of open-volume defects with a distribution of different sizes is expected. Moreover, lifetime values of positron trapped in these defects can be influenced by the presence of niobium and/or oxygen atoms in the Mg matrix. To evaluate this influence, *ab initio* calculations were performed.

The procedure used in a previous paper[14] for the calculation of positron lifetime in vacancy clusters in pure Mg was adopted here. We have used the free available Doppler program developed by the Electronic Properties of Materials Research Group at the Helsinki University of Technology.[66] In particular, we have applied a two-component density functional theory (DFT) in which the electron density of the solid was approximated by the superposition of free-atom electron densities. The potential felt by the positron was constructed as a sum of the Coulomb and correlation potentials, respectively. Then, positron lifetimes were obtained as the inverse of the annihilation rates calculated as an overlap integral of the electron and positron densities plus a term that takes into account the electron-positron correlation function at the positron site.[67] This term is usually called enhancement factor. Positron lifetimes were calculated using the local density approximation (LDA) of the correlation energy (see details in Ref. 14). Besides, the Boronski- Nieminen (BN) approximation for the electron-positron enhancement factor was used.[68]

In the case of calculation of the positron lifetimes in bulk systems, only the Γ point of the Brillouin zone was considered. Instead, in the system containing vacancies positron lifetimes were calculated in the Γ and L points of the Brillouin zone (options allowed into the program Doppler).[66] In all positron calculations a mesh of 128 × 128 × 128 grid points was used.

Regarding the crystal structure of each studied system, for Mg we have used the orthorhombic unit cell with four atoms as a basis specified by a lattice parameter $a = 3.21$ Å, $b = 1.30a$, and $c = 1.23a$. The calculations were performed with a supercell of 144 atoms (4 × 3 × 3 unit cells) without atomic position relaxation. The Mg-doped structures were generated by replacing one Mg atom with another atom as a substitutional impurity; that is, the Mg-Nb supercell contains 143 Mg atoms and 1 Nb atom. On the other hand, a monovacancy ($\square_1$) in the pure and doped Mg systems was created by removing one Mg atom located at the center of the cell or in a position corresponding to one of the first neighbors of the impurity atom. As we already reported for pure Mg, the calculation overestimates the positron lifetime in Mg bulk by

TABLE II. Calculated positron lifetimes in pure Mg, in Nb-doped Mg, and O-doped Mg and in the same structures but containing a vacancy. The difference and the relative difference of the lifetimes in doped Mg with respect to the lifetime in pure Mg are given in columns three and four, respectively. The same for the lifetimes of positron annihilating into a vacancy decorated by Nb or O, but with respect to the lifetime of positron trapped into a vacancy in pure Mg.

System	Lifetime (LDA) (ps)	Differences (ps)	Relative differences (%)
Mg_{144}	233		
$Mg_{143}Nb_1$	232	− 1	− 0.4
$Mg_{143}O_1$	229	− 4	− 1.5
$Mg_{143}\square_1$	298		
$Mg_{142}\square_1Nb_1$	294	− 4	− 1.3
$Mg_{142}\square_1O_1$	288	− 10	− 3.2

5 ps (experimental value of 218 ps) and in a monovacancy in Mg (298 ps against the experimental value of about 245 ± ps).[14]

For the present work, calculations pointed out that the presence of Nb or O atoms in the Mg matrix decreases the positron lifetime with respect to that of the matrix. This decrement is higher in the case of positron annihilated into a vacancy having as a first neighbor a Nb or O atom (see Table II).

2. Lifetime results

PALS measurements were meaningful for the bulk property of the studied material for the following reasons: (i) At the measured positron implantation energy ($E > 12$ keV) the mean lifetime $\bar{\tau}$ measured in each sample was constant, within the statistical scatters; and (ii) in the undefected Mg sample, the positron diffusion length resulted to be about 70 nm; therefore, for the spectra measured at energies higher than 12 keV the surface contribution can be neglected. In the following, the presented positron lifetimes τ_i and their associated intensities I_i are an average of three values measured at 14, 16, and 18 keV, equivalent to an implantation depth >1.2 μm.

Values of the positron lifetimes and their associated intensities obtained from the analysis of Nb-doped samples measurements are shown in Table III. For a comparative discussion, in the same table are also presented lifetime data for undoped Mg samples. These data were taken from Ref. 14.

PALS spectra were decomposed into three or four positron lifetime components, except for the sample #0HC in which the spectra were satisfactorily decomposed using two lifetimes. In all PALS spectra, a long-lived lifetime component of about 1–2 ns and a very low intensity (about 1%–2%) was observed. This long lifetime can be associated with positronium formation and annihilation in large voids likely formed at the Pd/Mg and Pd/Mg + Nb interfaces.[69]

In the case of the samples corresponding to the series #n and #nLC, in all PALS spectra a free fitting analysis revealed the presence of a lifetime component $\tau_3 = 380 \pm 10$ ps. Analysis of all the spectra obtained measuring the samples of the #nHC series clearly revealed a lifetime component $\tau_3 = 415 \pm 15$ ps.

In a second analysis, the lifetime τ_3 was fixed at 380 ps (series #n and #LC) and 415 ps (series #HC). Due to their values, this lifetime component can be ascribed to positron annihilation in vacancy clusters with equivalent sizes of 8 and 15 vacancies in pure Mg, respectively.[14]

The shortest lifetime τ_1 in the #LC and #n series can be considered as a reduced bulk lifetime for Mg,[70] as well as for the Nb-doped Mg system. In the case of the samples with low Nb content, for the as-deposited state and until the 4th cycle, the first lifetime components present short lifetime values (<60 ps) and intensities around 10%. For the sample submitted to the 8th sorption cycle, τ_1 disappears. PALS spectra for the series with high Nb content were well fitted without the shortest lifetime component τ_1.

In the case of the second lifetime τ_2, this component can be associated with positron annihilations in open-volume defects with sizes equivalent to one or two vacancies of Mg.[14] The presence of Nb in the proximity of open-volume defects reduces the lifetime with respect to that corresponding to positrons trapped into defects with the same size but in pure nanocrystalline Mg.

The τ_2 values for the #LC series monotonically decrease from 282 ps (as-deposited sample) to 214 ps after the 8th cycle. The associated intensity I_2 drastically decreases from 74% to 33% after the 1st cycle, and then its value increases again reaching a final value of 48% (see Fig. 8).

In the as-deposited high Nb content sample we observe that almost all positrons annihilate in defects with a lifetime τ_2 of 296 ps indicating a positron saturation trapping signal. With cycling, this lifetime decreases from 263 to 204 ps after the 2nd cycle and remains almost constant for the 4th cycle; finally, τ_2 slowly increases to 229 ps for the 8th cycle. In correspondence, the intensity I_2 first decreases from 57% (1st cycle) to 41% (2nd cycle), followed by an important increase reaching a value of 60% (8th cycle) (see Fig. 8). In the #n series the second component, characterized by a lifetime of about 260 ps in the 1st and 2nd cycle, disappears after the 4th cycle.

As can be seen in Fig. 8, the evolution of the intensity I_3 (corresponding to positron annihilation into vacancy clusters) with sorption cycles is similar for all the three series of the studied samples. This intensity monotonically increases up to the 2nd cycle, then reaches an almost constant value.

3. CDB results

To have an insight from the CDB measurements, the relative differences G^o of the measured momentum distribution spectra can be described as a linear combination of the relative momentum distributions G_i^o, defined in Eq. (2), and characterizing the positron annihilation in the different states i:

$$G^o = G^o_{\mathrm{Mg}} f_{\mathrm{Mg}} + G^o_{\mathrm{Nb}} f_{\mathrm{Nb}} + G^o_{v-\mathrm{Mg}} f_{v-\mathrm{Mg}} + G^o_{vc-\mathrm{Mg}} f_{vc-\mathrm{Mg}} + G^o_{\mathrm{O}} f_{\mathrm{O}}. \quad (6)$$

The G^o for each sample (i.e., for Mg and the Nb-doped Mg samples in the condition as-deposited or cycled) was fitted using as free parameters the fractions f_i of positrons annihilating with magnesium, niobium, and oxygen electrons, respectively, and annihilating into vacancylike defects and/or

TABLE III. Positron lifetimes and their associated intensities for (a) as-deposited and cycled Mg samples. Data were taken from Ref. 14, (b) as-deposited and cycled Nb-doped Mg samples with low Nb content, (c) as-deposited and cycled Nb-doped Mg samples with high Nb content. The error associated with the intensities is ±1%.

Sample	τ_1 (ps)	τ_2 (ps)	τ_3 (ps)	I_1 (%)	I_2 (%)	I_3 (%)
			Mg films			
#0	80 ± 4	241 ± 4	380	12	67	21
#1	125 ± 2	263 ± 2	380	26	29	44
#2	122 ± 2	260 ± 2	380	25	25	49
#4	165 ± 3		380	42		57
#8	177 ± 3		380	50		49
			Nb-doped Mg samples with low Nb content			
#0LC	45 ± 2	282 ± 1	380	8	74	18
#1LC	64 ± 2	256 ± 1	380	13	33	53
#2LC	47 ± 5	229 ± 3	380	12	33	55
#4LC	41 ± 6	222 ± 2	380	8	37	52
#8LC		214 ± 2	380		48	49
			Nb-doped Mg samples with high Nb content			
#0HC		296 ± 1			99.5	
#1HC		263 ± 2	415		57	42
#2HC		204 ± 1	415		41	58
#4HC		207 ± 5	415		48	51
#8HC		229 ± 3	415		60	39

vacancy clusters. The values of the fraction f_i obtained from the best fitting of the data are reported in Table IV.

In the literature a relationship between the intensity associated with a lifetime component corresponding to positron annihilation in vacancylike defects and the fraction f_i [71,72] has been reported as follows:

$$f_i = \frac{I_i(\tau_i - \tau_1)}{\tau_i},$$

where τ_1 is the reduced bulk lifetime and the τ_i are the positron lifetimes corresponding to positrons annihilated in the different kinds of open-volume defects. As an example, in thermal equilibrium measurements in pure metals only one kind of defect is generally found, that is, monovacancies.

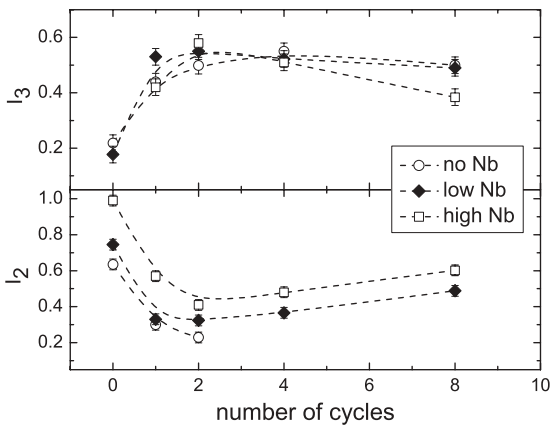

FIG. 8. Evolution of the lifetime intensities I_2 and I_3 as a function of the number of sorption cycles. I_2 and I_3 correspond to lifetimes τ_2 and τ_3 characterizing positrons annihilation in vacancylike defects and vacancy clusters, respectively. See also Table III.

To take into account this equation it is necessary that the positron standard trapping model (STM) be valid. As already discussed in Ref. 14, the STM is not the adequate model to analyze positron annihilation in the nanostructured materials studied in the present work. Therefore, only a direct proportionality between I_i and f_i can be assumed.

In Fig. 9, the G^o curves for the pure Mg (column on the left) and Mg doped with high-Nb-content samples (column on the right) are reported. The behavior of G^o curves for the Mg doped with low Nb content are similar to those of the samples with high Nb content, except for the f_i values; for this reason, they are not presented here. The solid lines through the experimental points are the best fits to the data.

Despite the high complexity of the studied systems, it must be outlined that the adopted procedure gives (i) good fits and reliable trends of the positron fraction when compared with the lifetime data and (ii) experimental evidence on the presence of vacancylike defects near the Nb aggregates. The obtained fractions of positron annihilating into vacancylike defects and into vacancy clusters must be assumed as indicative and with some care due to the intrinsic limits of the fingerprints (characteristic G_i^o curves) adopted for the fitting procedure.

It is worth mentioning that it is very difficult to obtain reference samples that contain only a specific open-volume defect for extracting its characteristic G_i^o curve. With these constraints, the $f_{v-\mathrm{Mg}}$ would represent the positron annihilation in vacancylike defects with a size equivalent to a monovacancy in pure Mg, while $f_{vc-\mathrm{Mg}}$ would represent positron annihilations in vacancy clusters which may have different sizes.

In pure Mg, the main feature is the disappearance, after the 4th cycle, of positron annihilations with the valence electrons of vacancylike defects. This result is in agreement with the disappearance of the second lifetime component τ_2. For the

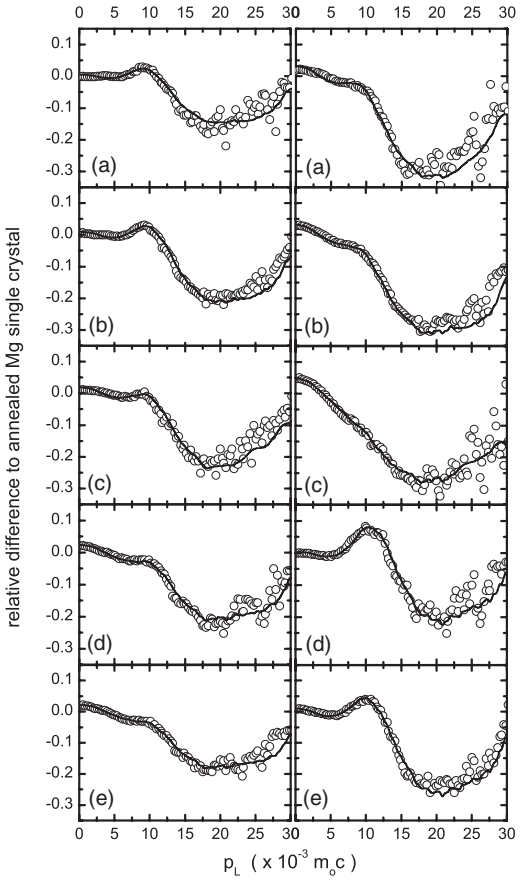

FIG. 9. CDB relative difference curves obtained measuring pure magnesium samples (left column) and samples with high Nb content (right). (a) As deposited, #0, #0HC sample; (b) after the 1st cycle, #1, #1HC; (c) after the 2nd cycle, #2, #2HC; (d) after the 4th cycle #4, #4HC; and (e) after the 8th cycle, #8, #8HC. Solid lines represent the fitting of the CDB data (see text).

#0, #1, and #2 samples, the bump located around $p_L = 10 \times 10^{-3}\ m_o c$, with its centroid at $p_L < 10 \times 10^{-3}\ m_o c$, is mainly due to positron annihilations into monovacancies. As can be seen, its intensity decreases as positron annihilations into vacancy clusters increases and the contribution of $G^o_{vc-\mathrm{Mg}}$ becomes more significant.

In all samples of the series, an almost constant fraction of positrons annihilates with oxygen electrons and contributes to the peak: As mentioned above, oxygen is dispersedly present in the sample with a concentration lower than about 10^{-4} at.$^{-1}$. Nevertheless, it cannot be excluded that oxygen atoms decorate some open-volume defects. Since vacancies disappear after the 2nd cycle and positron annihilations with oxygen are always present, it can be inferred that oxygen could most probably decorate some vacancy clusters.

In the samples #0HC and #1HC [see Figs. 9(a) and 9(b), right column], the bump with centroid at $p_L < 10 \times 10^{-3}\ m_o c$ is correlated with the presence of an important fraction (about 28% and 19%, respectively) of positrons annihilating with vacancylike defects. It must also be noted the increase of the G^o curve near $p_L = 0$. Both behaviors are clearly observed in the fingerprint corresponding to positrons annihilated into vacancylike defects (see Fig. 1). After the 2nd cycle [Fig. 9(c), right column], the main component is the fraction of positron annihilating into vacancy clusters (57%) and near $p_L = 0$ the G^o curve has a higher value than the previous ones. Then, this component decreases up to a value of ~40%. After the 4th and the 8th cycles, a clear peak around $11.8 \times 10^{-3}\ m_o c$ appears [see Figs. 9(d) and 9(e)], which can be related to the appearance of a fraction of positrons annihilated with Nb electrons.

In the as-deposited sample and after the 1st cycles, a signal of positron annihilation with oxygen electrons is revealed; after the 2nd cycle this signal strongly decreases. In this case, from the fitting procedures only an upper limit of f_O can be obtained; the values are given in Table IV. From EXAFS measurements this signal can be attributed to the presence of O-Nb correlations, but some contributions from Mg-O bonds cannot be excluded.

TABLE IV. Fraction f obtained by fitting the relative difference of the one-momentum distribution CDB experimental curves to that of pure Mg. In order: fraction of positron annihilated with electrons of Mg f_{Mg}; electrons in vacancy clusters $f_{vc-\mathrm{Mg}}$ and in monovacancies $f_{v-\mathrm{Mg}}$; electrons of O inclusions f_{O} (see text) and of Nb f_{Nb}. The error bars associated with f_i are $\pm 0.5\%$.

	CDB fractions f_i (%)				
Sample	f_{Mg}	$f_{vc-\mathrm{Mg}}$	$f_{v-\mathrm{Mg}}$	f_{O}	f_{Nb}
Mg films					
#0	55	14	18	13	
#1	42	23	17	18	
#2	43	29	14	14	
#4	45	41		14	
#8	55	35		10	
Nb-doped Mg samples with low Nb content					
#0LC	35	7	41	17	
#1LC	30	40	17	13	
#2LC	34	41	9	16	
#4LC	45	34		<2	$17 < f_{\mathrm{Nb}} < 1$
#8LC	48	32		<2	$16 < f_{\mathrm{Nb}} < 18$
Nb-doped Mg samples with high Nb content					
#0HC	25	34	28	13	
#1HC	30	40	19	11	
#2HC	39	57		<1	$3 < f_{\mathrm{Nb}} < 4$
#4HC	43	40		<5	$12 < f_{\mathrm{Nb}} < 17$
#8HC	33	39	13	<2	$13 < f_{\mathrm{Nb}} < 15$

4. *Vacancylike defects evolution*

Information about sites, decorations and concentrations of vacancylike defects and vacancy clusters after the H_2 sorption cycles can be obtained from the analysis of the positron lifetime values obtained from *ab initio* calculations in correlation with PALS and CDB experimental results (data reported in Tables III and IV, respectively). As already mentioned, from the constrained analysis of the PALS spectra, three lifetime components were found: a reduced bulk lifetime (τ_1), a second component associated with vacancies (τ_2), and a third one coming from positrons annihilated into vacancy clusters (τ_3).

In the as-deposited samples of undoped Mg, the very short reduced bulk lifetime τ_1 points out that a fraction of positrons

is efficiently trapped during its diffusion motion inside the Mg nanograins. From this evidence, it was inferred[14] that a fraction of vacancylike defects, characterized with a positron lifetime of 241 ± 4 ps, is stabilized by dislocations located into the defected nanograins (i.e., intragranular positron trapping sites). Vacancy clusters are expected to be more probably located at grain boundaries. The addition of Nb to the as-deposited samples produces more vacancylike defects. Specifically, the #0LC sample contains more vacancylike defects and their sizes are larger than that of a monovacancy (i.e., 74% vs 67% and 282 ps vs 241 ps, respectively). Moreover, since a third lifetime component is also revealed, there is a presence of some vacancy clusters as well. In the #0HC sample, only one positron lifetime could be obtained from the decomposition of the spectra, and it can be thus concluded that there exists a positron annihilation regime under saturation conditions. However, from the lifetime absolute value (296 ± 1 ps) it results that this component is most probably an average of contributions coming from positrons annihilated into vacancylike defects and vacancy clusters too (see also Table IV).

In the undoped Mg films, the density of vacancylike defects progressively decreases with the H_2 sorption cycles and after the 4th cycle these defects disappear. Due to their high mobility,[73] a fraction of intragranular vacancies are supposed to migrate toward grain boundaries in which they could coalesce to form vacancy clusters. The gradual disappearance of the intragranular vacancies is indirectly confirmed by a progressive increase of the reduced bulk lifetime. In the undoped samples there is a strong increase in the desorption kinetics after the 4th sorption cycle[14] that can be correlated with the increase of the vacancy clusters formed at grain boundaries (see Table IV). From the CDB results reported in Table IV for the same undoped samples, it can also be seen that an almost constant fraction of positrons are annihilated with electrons of O atoms. This signal still remains when after the 4th cycle vacancylike defects disappear and the desorption kinetics increases. Therefore, it could be concluded that oxygen in the Mg matrix does not participate in the hydride-to-metal phase transformations. This assertion is also supported by the fact that the strength of the Mg-O bond is much higher than that of the Mg-H.[74]

Cycling the #LC and #HC series samples, the following was observed. (i) Up to the 2nd cycle, the intensity of the second lifetime component I_2 and the fraction of positrons annihilated into vacancies of Mg $f_{v-\mathrm{Mg}}$ strongly and monotonically decrease; this behavior is similar to that observed for samples of the pure Mg series (see bottom panel of Fig. 8 and Table IV), and it can be attributed to the disappearance of a fraction of vacancylike defects. (ii) After the 4th cycle, in pure Mg samples this kind of defect disappears while in the samples containing Nb an increase of vacancylike defects is observed with a concomitant detection, in the analysis of the CDB distributions, of a signal coming from positrons annihilated with Nb electrons (see Table IV).

The decrease of vacancylike defects in the Nb-doped Mg samples is concurrent with the increase of vacancy clusters (see Fig. 8). From the 4th cycle on, in pure Mg and Nb-doped Mg samples, the intensity of the lifetime component associated with positron annihilated in vacancy clusters (I_3) has a similar trend. Looking at the behavior of vacancies observed in pure Mg (and also for the samples of the #LC and #HC series) up to the 2nd cycle, it can be inferred that a fraction of vacancylike defects migrates toward grain boundaries where they coalesce, increasing the concentration of vacancy clusters.

The increase of the concentration of vacancylike defects after the 4th cycle (see I_2 in Fig. 8) and a clear signal coming from positron annihilated with Nb electrons (see f_{Nb} in Table IV), would indicate that positrons are preferentially annihilating in misfit regions at the bcc Nb aggregates/hcp Mg matrix interfaces. This assertion is reinforced by the fact that when analyzing positron affinities A_+ (compare -6.18 eV for Mg with -2.93 eV for Nb)[75] in an undefected Nb-Mg interface, positrons must be more strongly attracted by Mg atoms than the Nb ones; therefore, the most probable way by which positrons could probe a significant Nb signal is the presence of vacancylike defects located at the Nb/Mg interfaces.

When comparing the fraction of positrons annihilated with Nb, it is found that for the #HC samples this signal appears before that of the #LC samples. This finding is in agreement with the EXAFS results, showing that the Nb aggregation process is delayed in #LC series.

After the 2nd cycle, in the #LC and #HC series τ_2 decreases below 245 ± 5 ps, which is the experimental positron lifetime of a vacancy in pure Mg. In the literature, positron lifetime values of ∼120 and ∼210 ps corresponding to positron annihilation in pure Nb and in a monovacancy of Nb, respectively, were reported.[72] Accordingly, the above-mentioned decrease of the second lifetime component can be related to the presence of Nb atoms near the vacancy site. This is supported by the calculated positron lifetime in a Mg vacancy decorated with a Nb atom (see Table I); in fact, this lifetime decreases in comparison with that calculated for pure Mg.

Following the same procedure described in Ref. 14 by the authors of the present work, into the frame of the positron diffusion trapping model (DTM),[76] the concentration of vacancylike defects C_v and the specific positron trapping rate at the grain boundaries α was estimated. It must be pointed out that in this model a competitive positron trapping at intragranular point defects and at grain boundaries in polycrystalline materials is assumed.[77,78]

For the data reported here, the DTM could be applied only to the lifetime data corresponding to the #0LC, #1LC, #2LC, and #4LC samples. The model could not be applied in the case of the sample #8LC and for all the samples of #HC series because in these cases all positrons become trapped into defects (saturation condition); that is, this behavior is reflected in the absence of a reduced bulk lifetime.

The input data for the analytical solution of the DTM were the positron diffusion in pure Mg $D_+ = 22 \times 10^{-6}$ m^2/s,[14] the specific trapping rate at vacancies $\nu = 4 \times 10^{14}$ s^{-1},[77] and a grain radius of 50 nm as experimentally obtained. As a result, C_v values of 3×10^{-5} at.$^{-1}$, 9×10^{-6} at.$^{-1}$, 8×10^{-6} at.$^{-1}$, and 1×10^{-5} at.$^{-1}$ and α values of 45, 110, 115, and 110 m/s were calculated for the #0LC, #1LC, #2LC, and #4LC samples, respectively. It must be pointed out that when α increases it means that there is an enhanced positron trapping at grain boundaries. The C_v values calculated are about three

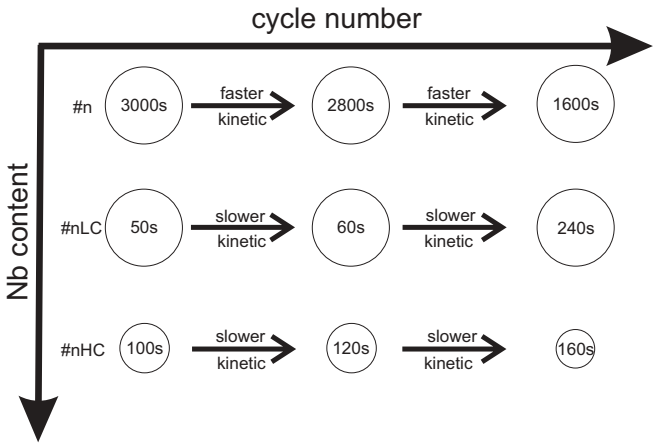

FIG. 10. Scheme of the H_2 desorption kinetics at 623 K as a function of the Nb content and of the number of H_2 sorption cycles (see text). The values of $\tau_{\frac{1}{2}}$ are reported. Left column, 2nd cycle. Central column, 5th cycle for undoped Mg sample and 3rd cycle for the Nb-doped Mg samples. Right column, stationary condition. The dimension of the circles represents the Mg grain size (large circle, ~80 nm; small circle, ~50 nm). Pure Mg: large circle, ~100 nm. Nb-doped Mg, large circle, ~80 nm, small circle, ~50 nm.

times higher than those we obtained for the #0, #1, and #2 samples;[14] values of α are similar for the as-deposited #0LC and #0 samples. The value of this parameter for the #1LC and #2LC is about twice those calculated for the #1 and #2 samples.

These atomic fraction values are at least 10 times higher than that of equilibrium at $T = 623$ K, which was estimated to be in the 10^{-8} to 10^{-7} at.$^{-1}$ order using the well-known relationship $C_v = A \exp(-E_f/kT)$ and knowing that the vacancy formation energy E_f in Mg is between 0.8 and 0.9 eV (see Ref. 79 and references therein).

PAS results can be summarized as follows.

(i) The addition of Nb atoms in the Mg matrix produces a system enriched in vacancylike defects, whose concentration increases by increasing the dopant content.

(ii) Up to the 2nd cycle, as already observed in pure Mg,[14] a fraction of intragranular vacancylike defects migrates clustering at grain boundaries. The Nb agglomeration process is assisted by vacancylike defects.

(iii) In the Nb-doped Mg samples, and when stationary conditions are reached, vacancy clusters are located at grain boundaries. The presence of Nb aggregates promotes the localization of vacancylike defects at the bcc Nb/hcp Mg interfaces.

D. Mechanism of hydrogen desorption

The change in the nanocomposite structure observed by PAS and EXAFS in the sample submitted to the 1st sorption cycle is due to the thermal treatment applied during the activation process as well as to the phase transformations occurred in the 1st cycle. After this cycle, the vacancylike defect evolution and the Nb aggregation are connected with the H_2 sorption process.

A schematic on the evolution of the H_2 desorption process is presented in Fig. 10. For comparison, the evolution in pure Mg (#n) is also reported. The horizontal axis describes the progressive increase of the H_2 sorption cycles, while the vertical axis the increase of the Nb content. Arrows indicate the status of the H_2 desorption kinetics. The dimension of the circles represents the average size of the Mg grains; inside these circles, values of the half desorption times $\tau_{\frac{1}{2}}$ are reported. In particular, we report the status of the systems after three steps: (a) 2nd cycle, when the samples are not completely hydrogenated; (b) 3rd cycle for #LC and #HC, when the samples are nearly completely hydrogenated (5th cycle for the undoped Mg sample); and (c) when stationary conditions are reached.

From a qualitative point of view, (i) when comparing the stationary conditions, with the increase of the Nb content an improvement of the desorption kinetics is observed, and (ii) in the initial cycles, the characteristic time is longer in the sample with higher Nb content.

It is known that in hydride-forming materials a grain size in the nanometer range can have a strong effect on the velocity of the hydrogen sorption process[1–4] because grain boundaries act as fast diffusion channels for H atoms and facilitate the H transport process. In the present doped samples, XRD analysis (see inset in Fig. 5) shows that for the #LC samples the average Mg grain size does not change, while in the #HC samples a grain fragmentation accompanying the progressive Nb clustering is observed.

Two points indicate that the observed change in the H_2 sorption kinetics is not related to the Mg grain size: (i) In the film samples with high Nb content, the progressive grain fragmentation would speed up the H_2 desorption process,[1–4] but this is not observed; and (ii) in the samples with low Nb content, the grain size remains stable while the kinetics progressively becomes slower.

Since the change in the H_2 sorption kinetics is not caused by the change of the Mg grain size, a concomitant contribution of vacancylike defects, vacancy clusters, and bcc Nb aggregates can be expected. We now discuss the role of vacancies.

In pure Mg (grain size ~100 nm), the hydrogen desorption kinetics accelerates with successive H_2 sorption cycles; that is, the half desorption time decreases from ~3000 to ~1600 s, and also in this case a grain refinement was not observed (see Fig. 10).[14] It was also reported that the crystalline quality of the grains improves. When stationary conditions are reached, the Mg structure is formed by undefected grains, while vacancy clusters (atomic fraction $C_{vc} = 2 \times 10^{-6}$ at.$^{-1}$) are located at the grain boundaries.[14] Thus, the faster H_2 desorption kinetics was attributed to the role of the vacancy clusters which assist the Mg nucleation process in the hydride-to-metal phase transformation by reducing the strain term in the energy barrier for the formation of the critical Mg nuclei in the MgH_2 matrix.

The addition of Nb atoms to the Mg layers catalyzes the H_2 desorption process. As a result, the half desorption time decreases by at least one order of magnitude. Contrarily to what happens in the undoped Mg, in the doped samples the half desorption time increases with cycling although the vacancy-cluster dynamic is the same as that observed for the undoped sample (see Fig. 8). As a consequence, the formation of vacancy clusters in doped samples is not the driving mechanism in worsening the desorption kinetics.

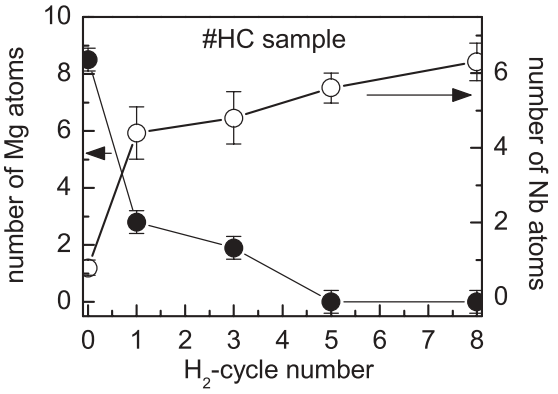

FIG. 11. Number of Nb atoms and Mg atoms in the average Nb site (within a radius of 3.5 Å) as from EXAFS for the #HC samples: The progressive Nb clustering is evident, characterized by an increase (decrease) of the Nb (Mg) population in the Nb site.

About the vacancylike defects, we observed that they do not disappear after the 2nd cycle. In fact, their content increases with the successive cycles and they are found to decorate mainly the Nb bcc clusters. The progressive Nb clustering occurs at the expense of the small Nb aggregates (not bcc-like clusters) and the Nb dispersed fraction. In the following, we analyze their contribution to the increase of the half desorption time. To this aim, from the EXAFS data obtained for the #HC films we have evaluated the number of Nb atoms populating the average Nb sites within a radius of 3.5 Å. This number is reported in Fig. 11 as a function of the H_2 sorption cycle. In the same figure, the number of Mg atoms in the same region is also reported. The progressive Nb clustering is evidenced by the increase of the Nb population and by the decrease of the Mg one. The Nb clustering with successive H_2 cycles follows about the same trend as the Mg strain release in similar samples.[50] It suggests that a high concentration of Nb atoms dispersed into the matrix and strongly correlated with it (i.e., with a definite Mg-Nb correlation) is the origin of the high Mg strain level.

The data of Fig. 11 can be correlated with the H_2 desorption rate as measured for the #HC films after successive sorption cycles. The fastest H_2 desorption occurs during the first steps of the Nb clustering when the Nb population consist of small Nb aggregates and/or by the dispersed Nb fraction.

Let us compare now the desorption kinetics of the #LC and #HC series. In the 1st cycles, the desorption kinetics of the #LC samples is faster than that of the #HC films and it becomes slower after about 8 cycles. In particular, at the 2nd and 3rd cycles the characteristic desorption time is significantly shorter for the #LC films (∼60 s) than for the #HC ones (∼120 s), despite the lower catalyst concentration. Correspondingly, while in the #HC films large bcc-like clusters (size of at least few nm) are already formed, in the #LC samples only the signal coming from the small Nb aggregates (size ∼1 nm) can be detected. Although this result suggests that the rapid desorption kinetics would be connected with the presence of the small Nb aggregates, a role of the dispersed fraction, characterized by a definite Nb-Mg distance of about 3.1 Å in both #HC and #LC films series (see Table I), cannot be excluded.

Recent theoretical calculations suggest, in fact, that TM elements in substitutional sites of MgH_2 lower the hydride stability, favoring a faster desorption kinetics.[18–21] In presence of different Nb-related phases (Nb clusters and dispersed Nb atoms), the coordination number measured by EXAFS for the Mg shell is the number of Mg atoms in the average site of dispersed Nb times the fraction of dispersed Nb. So, in both #HC and #LC samples series, considering that in the as-deposited films the dispersed fraction is less than one because a part of Nb forms aggregates, on average each Nb atom dispersed into the matrix coordinates likely more than 9 Mg atoms, and the site of dispersed dopant is similar in both #HC and #LC films (similar coordination number and radius for the Mg shell). For comparison, in a Mg crystal each Mg atom coordinates 12 Mg atoms at a distance of about 3.20 Å. To evaluate the effectiveness of the dispersed Nb fraction in driving the H_2 desorption, consider the coordination number of the Mg shell: With respect to the as-deposited case, after 3 cycles it is reduced to 1/5 (1/2) for the #HC (#LC) films, pointing out that the fraction of Nb dispersed into the Mg matrix is correspondingly reduced to 1/5 (1/2). Now, if we assume that the absolute Nb concentration in the #LC films is about one-third of the one in #HC films it comes out that, after 3 cycles, the absolute concentration of dispersed Nb atoms is about the same for the #HC and #LC films; but the H_2 sorption process is much faster in the #LC film than in the #HC one. This shows that the faster H_2 kinetics observed in the #LC films is mostly driven by the small Nb aggregates rather than by the Nb dispersed fraction.

In the successive cycles, the Nb aggregation process in bcc-like clusters proceeds and the site of the dispersed Nb fraction becomes extremely disordered; the Nb connection with the matrix is progressively lost. This is compatible with the presence of the dispersed Nb atoms close to the Mg grain boundaries where a larger variety of sites is likely accessible.

Our results suggest that small Nb aggregates are effective for a fast H_2 sorption kinetics. This is likely related to the role of the interface between niobium and the MgH_2 matrix that acts as a preferential nucleation site for metallic Mg in the hydride-to-metal phase transformation.

For a defined Nb metallic concentration, the presence of small aggregates has an important advantage. Small aggregates greatly extend the region of the dopant-matrix interfaces, thus increasing the number of sites for heterogeneous nucleation, well distributed in the Mg matrix, with likely a large fraction of atoms located in highly reactive special positions (like steps, edges, corners). This optimal distribution permits the prompt onset of a connected network for fast H migration, formed by Mg domains nucleated at the niobium-matrix interfaces.[7,11–13]

The progressive Nb clustering is detrimental for the velocity of the H_2 desorption process in both the #LC and the #HC samples. This effect is particularly evident in the #LC samples: Under stationary conditions of the H_2 desorption kinetics, the typical desorption time increases by a factor of 4 (∼240 s while at the 3rd cycle it was ∼60 s). EXAFS and PAS analyses indicate a concomitant aggregation of Nb bcc clusters and the appearance of vacancylike defects near Nb evidences that vacancylike defects are mostly localized at the bcc Nb-Mg interfaces.

We can thus present the following description of the #LC and #HC samples when stationary conditions of the H_2 desorption kinetics are reached. Samples consist of a nanostructured Mg matrix in which a fraction of dopant is atomically

dispersed and a fraction is forming bcc nanoclusters. Voidlike defects are in the form of monovacancies localized at the interfaces between the Nb clusters and the Mg matrix and in the form of vacancy clusters located at the Mg grain boundaries.

In samples showing stationary H_2 desorption conditions, other TM additives immiscible with Mg, as Fe, Zr,[11] or Ti[80,81] were found to have comparable catalytic effects to that of Nb when it aggregates in nanoclusters. These TM elements have different electronegativity values, electronic configurations, and, at the examined temperature of 623 K, form different compounds with hydrogen: The H solubility is negligible in Fe; H form a random interstitial alloy in bcc Nb and a stable phase with Zr, δ phase with a fcc structure. Detailed and comparative studies on the distribution and size of the TM aggregates and on the distribution of vacancylike defects in doped Mg samples in stationary conditions will be needed to determine if the acceleration of the kinetics with respect to the pure Mg, depends on the electronic structure at the TM/Mg interface or only on the size of the aggregates and their distribution inside the Mg matrix.

IV. CONCLUSIONS

EXAFS and PAS techniques were used to monitor the progressive clustering of the Nb atoms and the evolution of vacancy-like defects in Nb-doped Mg after successive H_2 sorption cycles. EXAFS spectroscopy revealed that the Nb additive forms (i) small aggregates where the bcc short-range order is not yet detectable (estimated size $\sim$1 nm) in the first H_2 sorption cycles and (ii) larger Nb bcc nanoclusters in the successive H_2 sorption cycles. Some Nb atoms remain dispersed in the matrix, likely in Mg grain boundary regions. This aggregation process is delayed in samples with low Nb content compared to samples with high Nb content. The strong Nb-Mg correlation observed in the as-deposited samples and pertinent to a dispersed fraction of the Nb additive progressively decreases and, after few H_2 cycles, the site of the dispersed Nb atoms is disordered, suggesting their segregation near the grain boundaries of the Mg matrix.

PAS analysis indicates the presence of intragranular vacancylike defects and of vacancy clusters located at the grain boundaries of the Mg matrix in the as-deposited sample. The H_2 cycling produces the following: (i) in the 1st 2 cycles, the decrease of the atomic fraction of intragranular vacancylike defects accompanied by the increase of the atomic fraction of vacancy clusters at the grain boundaries; (ii) after the 2nd H_2 cycle, the appearance of vacancylike defects located at the interface between the Nb aggregates and the Mg matrix.

The following conclusions were obtained.

(i) Under stationary conditions, the Mg nucleation process is controlled by vacancy-decorated bcc Nb nanoclusters rather than by vacancy clusters, as observed in undoped Mg samples.

(ii) The fast desorption kinetics observed in the 1st H_2 sorption cycles depends on the presence of the small Nb aggregates rather than on the dispersed Nb fraction.

(iii) At fixed Nb content, the small Nb aggregates are more effective as catalytic agent than the larger bcc Nb clusters.

(iv) The worsening of the H_2 desorption kinetics after successive H_2 cycles is due to the progressive Nb aggregation.

A possible route to limiting the Nb aggregation process is to increase the density of heterogeneous nucleation centers where the Ng aggregation occurs by, for example, introducing into the Mg matrix a second atomic additive, immiscible with Mg and having lower mobility than Nb in the host matrix. Preliminary experiments on Mg samples containing mixed Fe-Zr additives have shown a better H_2 desorption kinetics than that of Mg samples with the single Fe additive. Here XRD analysis revealed that the average size of the Fe nanoclusters was lower than that measured in the Mg samples with the single Fe additive. Reasonably, the Zr atoms segregated in grain boundaries[82] act as supplementary nucleation centers for the Fe aggregation forcing the formation of the Fe nanoclusters uniformly dispersed in the Mg matrix with reduced size.

ACKNOWLEDGMENTS

This work was partially supported by Ministerio de Ciencia, Tecnología e Innovación Productiva (Argentina), Agencia Nacional de Promoción Científica y Tecnologíca (Argentina) (PICT 2011-1088), Consejo Nacional de Investigaciones Científicas y Técnicas (Argentina) (PIP No. 114-200801-00444), Ministero degli Affari Esteri (Italia) (Project No. 82). The authors wish to acknowledge Gotfried Kögel for many stimulating discussions on the present paper. Beam time at FRMII is gratefully acknowledged. We acknowledge the European Synchrotron Radiation Facility and the Italian Collaborating Research Group for the provision of the synchrotron radiation facility. GILDA is a project jointly financed by CNR and INFN.

[1] L. Schlapbach and A. Zuettel, Nature (London) **414**, 353 (2001).
[2] J. Huot, G. Liang, and R. Schultz, Appl. Phys. A: Mater. Sci. Process. **72**, 187 (2001).
[3] G. Liang, J. Huot, S. Boily, and R. Schulz, J. Alloys Compd. **305**, 239 (2000).
[4] J. Huot, J. F. Pelletier, G. Liang, M. Sutton, and R. Schulz, J. Alloys Compd. **330–332**, 727 (2002).
[5] W. Oelerich, T. Klassen, and R. Bormann, Adv. Eng. Mater. **3**, 487 (2001).
[6] G. Barkhordarian, T. Klassen, and R. Bormann, J. Phys. Chem. B **110**, 11020 (2006).
[7] R. Checchetto, N. Bazzanella, A. Miotello, C. Maurizio, F. D'Acapito, P. Mengucci, G. Barucca, and G. Majini, Appl. Phys. Lett. **87**, 061904 (2005).
[8] O. Friederich, J. C. Sanchez-Lopez, C. Lopez-Cartes, T. Klassen, R. Bormann, and A. Fernandez, J. Phys. Chem. B **110**, 7845 (2006).
[9] J. F. Pelletier, J. Huot, M. Sutton, R. Schulz, A. R. Sandy, L. B. Lurio, and S. G. J. Mochrie, Phys. Rev. B **63**, 052103 (2001).
[10] H. G. Schimmel, J. Huot, L. C. Chapon, F. D. Tichelaar, and F. M. Mulder, J. Am. Chem. Soc. **127**, 14348 (2005).
[11] R. Checchetto, N. Bazzanella, A. Miotello, and P. Mengucci, J. Alloys Compd. **446–447**, 58 (2007).

[12]N. Bazzanella, R. Checchetto, A. Miotello, C. Sada, P. Mazzoldi, and P. Mengucci, Appl. Phys. Lett. **89**, 014101 (2006).
[13]N. Bazzanella, R. Checchetto, and A. Miotello, Appl. Phys. Lett. **85**, 5212 (2004).
[14]R. Checchetto, N. Bazzanella, A. Kale, A. Miotello, S. Mariazzi, R. S. Brusa, P. Mengucci, C. Macchi, A. Somoza, W. Egger, and L. Ravelli, Phys. Rev. B **84**, 054115 (2011).
[15]D. P. Broom, Int. J. Hydrogen Energy **32**, 4871 (2007).
[16]R. Checchetto, G. Trettel, and A. Miotello, Meas. Sci. Technol. **15**, 127 (2004).
[17]J. J. Rehr and R. C. Albers, Rev. Mod. Phys. **72**, 621 (2000).
[18]P. Larsson, C. Moyses Arujo, J. Larsson, P. Jena, and R. Ahuja, Proc. Nat. Acad. Sci. USA **105**, 8227 (2008).
[19]S. Li, P. Jena, and R. Ahuja, Phys. Rev. B **74**, 132106 (2006).
[20]Y. Song, Z. Guo, and R. Yang, Phys. Rev. B **69**, 094205 (2004).
[21]S. Er, D. Tiwari, G. A. de Wijs, and G. Brooks, Phys. Rev. B **79**, 024105 (2009).
[22]A. Ankudinov, B. Ravel, J. J. Rehr, and S. D. Conradson, Phys. Rev. B **56**, 7565 (1990).
[23]S. Valkealahti and R. M. Nieminen, Appl. Phys. A **35**, 51 (1984).
[24]P. Asoka-Kumar, K. G. Lynn, and D. O. Welch, J. Appl. Phys. **76**, 4935 (1994).
[25]M. J. Puska and R. M. Nieminen, Rev. Mod. Phys. **66**, 841 (1994).
[26]R. Krause-Rehberg and H. S. Leipner, *Positron Annihilation in Semiconductors*, Springer Series in Solid-State Sciences (Springer, Berlin, 1999).
[27]P. Kirkegaard, N. J. Pedersen, and M. Eldrup, *Computer program* PATFIT, RISO National Laboratory, Denmark, 1998.
[28]W. Egger, in *Physics with Many Positrons*, edited by R. S. Brusa, A. Dupasquier, and A. P. Mills Jr., (North-Holland, Amsterdam, 2010).
[29]C. Hugenschmidt in *Physics with Many Positrons*, edited by R. S. Brusa, A. Dupasquier, and A. P. Mills Jr., (North-Holland, Amsterdam, 2010).
[30]M. Alatalo, H. Kauppinen, K. Saarinen, M. J. Puska, J. Makinen, P. Hautojarvi, and R. M. Nieminen, Phys. Rev. B **51**, 4176 (1995).
[31]S. Szpala, P. Asoka-Kumar, B. Nielsen, J. P. Peng, S. Hayakawa, K. G. Lynn, and H. -J. Gossmann, Phys. Rev. B **54**, 4722 (1996).
[32]R. S. Brusa, W. Deng, G. P. Karwasz, and A. Zecca, Nucl. Instrum. Methods Phys. Res. Sect. B **194**, 519 (2002).
[33]A. Zecca, M. Bettonte, J. Paridaens, G. P. Karwasz, and R. S. Brusa, Meas. Sci. Technol. **9**, 409 (1998).
[34]C. Macchi, S. Mariazzi, G. P. Karwasz, R. S. Brusa, P. Folegati, S. Frabboni, and G. Ottaviani, Phys. Rev. B **74**, 174120 (2006).
[35]R. S. Brusa, G. P. Karwasz, N. Tiengo, A. Zecca, F. Corni, R. Tonini, and G. Ottaviani, Phys. Rev. B **61**, 10154 (2000).
[36]P. Hautojarvi, J. Johansson, A. Vehanen, and J. Yli-Kauppila, Appl. Phys. A **27**, 49 (1982).
[37]A. Somoza, M. P. Petkov, K. G. Lynn, and A. Dupasquier, Phys. Rev. B **65**, 094107 (2002).
[38]P. Folegati, A. Dupasquier, R. Ferragut, M. M. Iglesias, I. Makkonen, and M. J. Puska, Phys. Status Solidi C **4**, 3493 (2007).
[39]P. Folegati, I. Makkonen, R. Ferragut, and M. J. Puska, Phys. Rev. B **75**, 054201 (2007).
[40]A. Dupasquier, R. Ferragut, M. M. Iglesias, M. Massazza, G. Riontino, P. Mengucci, G. Barucca, C. Macchi, and A. Somoza, Philos. Mag. **87**, 3297 (2007).
[41]A. Calloni, A. Dupasquier, R. Ferragut, P. Folegati, M. M. Iglesias, I. Makkonen, and M. J. Puska, Phys. Rev. B **72**, 054112 (2005).
[42]M. Stadlbauer, C. Hugenschmidt, K. Schreckenbach, and P. Böni, Phys. Rev. B **76**, 174104 (2007).
[43]R. S. Brusa, M. Duarte Naia, A. Zecca, C. Nobili, G. Ottaviani, R. Tonini, and A. Dupasquier, Phys. Rev. B **49**, 7271 (1994).
[44]A. Somoza, M. P. Petkov, K. G. Lynn, and A. Dupasquier, Phys. Rev. B **65**, 094107 (2002)
[45]R. S. Brusa, C. Macchi, S. Mariazzi, G. P. Karwasz, W. Egger, P. Sperr, and G. Kögel, Phys. Rev. B **71**, 245320 (2005).
[46]R. S. Brusa, Phys. Status Solidi C **10**, 3614 (2007).
[47]M. Hakala, M. J. Puska, and R. M. Nieminen, Phys. Rev. B **57**, 7621 (1998).
[48]G. Liang, J. Huot, S. Boily, and R. Schulz, J. Alloys Compd. **305**, 239 (2000).
[49]J. W. Christian, in *The Theory of Transformation in Metals and Alloys*, 3rd ed. (Pergamon, London, 2002).
[50]P. Mengucci, C. Barucca, G. Majni, N. Bazzanella, R. Checchetto, and A. Miotello, J. Alloys Compd. **509**, S572 (2011)
[51]A. Balerna and S. Mobilio, Phys. Rev. B **34**, 2293 (1986).
[52]G. D'Agostino, A. Pinto, and S. Mobilio, Phys. Rev. B **48**, 14447 (1993).
[53]P. A. Montano, G. K. Shenoy, E. E. Alp, W. Schulze, and J. Urban, Phys. Rev. Lett. **56**, 2076 (1986).
[54]L. Goodwin and D. R. Salahub, Phys. Rev. A **47**, R774 (1993).
[55]V. Kumar and Y. Kawazoe, Phys. Rev. B **65**, 125403 (2002).
[56]H. Groenbeck, A. Rosen, and W. Andreoni, Phys. Rev. A **58**, 4630 (1998).
[57]R. FengZhu, W. Yuan-Xu, Z. Guang-Biao, W. Shu-Ke, and L. You-Hua, Chin. Phys. B **18**, 1491 (2009).
[58]S. K. Nayak, B. Rao, S. Khanna, and P. Jena, Chem. Phys. Lett. **259**, 588 (1996).
[59]C. Lekka and D. Papaconstantopoulos, Surf. Sci. **601**, 3937 (2007).
[60]R. R. Banerjee, E. A. Sperling, G. B. Thompson, H. L. Fraser, S. Bose, and P. Ayyub, Appl. Phys. Lett. **82**, 4250 (2003).
[61]A. R. Yavari, J. F. R. de Castro, G. Vaughan, and G. Heunen, J. Alloys Compd. **353**, 246 (2003).
[62]Y. Fukai, in *The Metal-Hydrogen System, Basic Bulk Properties* (Springer-Verlag, Berlin, Heidelberg, 2005).
[63]P. Bevington, in *Data Reduction and Error Analysis for the Physical Sciences* (McGraw-Hill, New York, 2003).
[64]A. Miotello, G. De Marchi, G. Mattei, P. Mazzoldi, and C. Sada, Phys. Rev. B **63**, 075409 (2001).
[65]G. De Marchi, G. Mattei, P. Mazzoldi, C. Sada, and A. Miotello, J. Appl. Phys. **92**, 4249 (2002).
[66]DOPPLER: A program to model positron states and annihilation in solids, Laboratory of Physics, Helsinki University of Technology (2003), [http://tfy.tkk.fi/epm/research/positron/dopplerdoc.pdf].
[67]T. Torsti, T. Eirola, J. Enkovaara, T. Hakala, P. Havu, T. Höynälänmaa, J. Ignatius, M. Lyli, I. Makkonen, T. T. Rantala, J. Ruokolainen, K. Ruotsalainen, E. Räsänen, H. Saarikoski, and M. J. Puska, Phys. Status Solidi B **243**, 1016 (2006).
[68]E. Boronski and R. M. Nieminen, Phys. Rev. B **34**, 3820 (1986).
[69]S. W. Eijt, R. Kind, S. Singh, H. Schut, W. J. Legerstee, R. W. A. Hendrikx, V. L. Svetchnikov, R. J. Westerwaal, and B. Dam, J. Appl. Phys. **105**, 043514 (2009).
[70]C. Corbel and P. Hautojärvi, in *Positron Spectroscopy of Solids*, edited by A. Dupasquier and A. P. Mills Jr., (North-Holland, Amsterdam, 1995).
[71]A. Calloni, A. Dupasquier, R. Ferragut, P. Folegati, M. M. Iglesias, I. Makkonen, and M. J. Puska, Phys. Rev. B **72**, 054112 (2005).

[72]J. Cížek, I. Procházka, S. Daniš, G. Brauer, W. Anwand, R. Gemma, E. Nikitin, R. Kirchheim, A. Pundt, and R. K. Islamgaliev, Phys. Rev. B **79**, 054108 (2009).
[73]P. Hautojarvi, J. Johansson, A. Vehanen, J. Yli-Kauppila, J. Hillairet, and P. Tzanétakis, Appl. Phys. A **27**, 49 (1982).
[74]Mark A. Shand, *The Chemistry and Technology of Magnesia* (Wiley Interscience, Hoboken, NJ, 2006), pp. 121.
[75]M. J. Puska and R. M. Nieminen, Rev. Mod. Phys. **66**, 841 (1994).
[76]Dupasquier, R. Romero, and A. Somoza, Phys. Rev. B **48**, 9235 (1993).
[77]B. Oberdorfer and R. Würschum, Phys. Rev. B **79**, 184103 (2009).
[78]H.-E. Schaefer, Phys. Status. Solidi A **102**, 47 (1987).
[79]H. Krimmel and M. Fahnle, Phys. Rev. B **62**, 5489 (2000).
[80]A. Baldi, R. Gremaud, D. M. Borsa, C. P. Baldè, A. M. J. van der Eerden, G. L. Kruijtzer, P. E. de Jongh, B. Dam, and R. Griessen, Int. J. Hydrogen Energy **34**, 1450 (2009).
[81]H. Leegwater, H. Schut, W. Egger, A. Baldi, B. Dam, and S. W. H. Eijt, Appl. Phys. Lett. **96**, 121902 (2010).
[82]P. Leicek, *Grain Boundary Segregation in Metals* (Springer-Verlag, Berlin, 2010).